

Towards variance-conserving reconstructions of climate indices with Gaussian Process Regression in an embedding space

Marlene Klockmann¹, Udo von Toussaint², and Eduardo Zorita¹

¹Institute for Coastal Systems - Analysis and Modelling, Helmholtz-Zentrum Hereon, Geesthacht, Germany

²Max Planck Institute for Plasma Physics, Garching, Germany

Correspondence: M. Klockmann (marlene.klockmann@hereon.de)

Abstract. We present a new framework for the reconstruction of climate indices based on proxy data such as tree rings. The framework is based on the supervised learning method Gaussian Process Regression (GPR) and ~~designed to preserve aims at preserving~~ the amplitude of past climate variability ~~and to~~. ~~It can~~ adequately handle noise-contaminated proxies and variable proxy availability ~~in over~~ time. To this end, the GPR is ~~performed formulated~~ in a modified input space, termed ⁵ ~~here~~ embedding space. We test the new framework for the reconstruction of the Atlantic Multi-decadal Variability (AMV) in a controlled environment with pseudoproxies derived from coupled climate-model simulations. In this test environment, the GPR outperforms benchmark reconstructions based on multi-linear ~~Principle Principal~~ Component Regression. On AMV-relevant timescales, i.e., multi-decadal ~~timescales~~, the GPR is able to reconstruct the true ~~magnitude amplitude~~ of variability even if the proxies contain a ~~realistic~~ non-climatic noise signal and become sparser back in time. Thus, we conclude that the embedded ¹⁰ GPR framework is a highly promising tool for climate-index reconstructions.

1 Introduction

Climate indices are important measures to describe the evolution of climate on regional, hemispheric or global scales in a condensed way. They reveal relevant timescales of climate variability and, in some cases ~~also relevant~~, ~~also~~ subspaces that are important for predictability. Paramount examples are the El Niño-Southern Oscillation, the North Atlantic Oscillation ¹⁵ and the Atlantic Multi-decadal Variability (AMV). To understand whether the typical timescales and magnitude of climate variability have been stationary over time or whether they have changed, e.g., with anthropogenic climate change, we need a long-term perspective on these climate indices. The index-timeseries must not only cover the historical period of the past 150 years but also the ~~preindustrial period of interest, e.g.,~~ ~~i.e.,~~ the past 1000 to 2000 years (~~Common Era~~). To obtain these long timeseries we need information from so-called climate proxies (e.g. tree rings, sediment cores) in combination with ²⁰ sophisticated statistical models to reconstruct the climate indices from the proxy data. We present a new machine-learning framework for climate-index reconstructions and test its skill for reconstructing the AMV.

The AMV is an important index that describes the North Atlantic climate variability on decadal and longer timescales. Different definitions of the AMV have been developed over time, but the basic definition relies on the low-pass filtered spatial average of sea surface temperature anomalies over the North Atlantic. Observations starting in about 1850 indicate that the

25 AMV varies on typical timescales of 30 to 60 years. The state of the AMV plays a key role for many relevant climate phenomena such as Arctic sea-ice anomalies (Miles et al., 2014), North American and European summer climate, Hurricane hurricane seasons and Sahel rainfall (Zhang and Delworth, 2006; Zhang et al., 2007).

30 The origin of the AMV remains a topic of active debate (see Zhang et al., 2019, for a recent review). One of the main questions is whether the variability is mainly induced by oceanic or atmospheric processes. Atmospheric simulations coupled to a slab ocean produced very similar spectra to the observed AMV, suggesting that the AMV could be generated purely from atmospheric variability (Clement et al., 2015). This is also called the red noise hypothesis, according to which the AMV is the red-noise response to atmospheric white-noise forcing. This hypothesis, however, is not compatible with other AMV features, as described in Zhang et al. (2019). A multi-variate AMV index suggests that the observed AMV is mainly driven by changes in the ocean circulation, especially the Atlantic Meridional Overturning Circulation (AMOC, Yan et al., 2019). This 35 does, however, not exclude a contribution of atmospheric processes because ocean-driven variability also includes coupled air-sea feedbacks (e.g., Garuba et al., 2018; Zhang et al., 2019).

40 A second main question is Both atmospheric as well as oceanic processes have been suggested as possible drivers of the AMV (Clement et al., 2015; Zhang et al., 2019; Yan et al., 2019; Garuba et al., 2018, e.g.). It is not clear, how much of the variability is due to internal AMV is generated by internal climate variability and how much results from the response to external changes in radiative is generated by changes in external radative forcing, i.e., through volcanic volcanic and anthropogenic aerosols, solar insolation and greenhouse gas changes. On the one hand, analyses of 20th century SST observations (Haustein et al., 2019) as well as preindustrial control simulations with coupled climate models (Mann et al., 2021) suggested a limited role for internally generated variability but rather advocate that the AMV is the result of competing anthropogenic forcing (aerosols and greenhouse gases) and volcanic forcing. On the other hand, the dominant role of the AMOC (Garuba et al., 2018) indicates 45 that a large part of the observed AMV is due to internally generated oceanic variability. (Haustein et al., 2019; Mann et al., 2021).

50 Given the dominant multi-decadal timescales of the AMV, the The observational period of approximately 150 years is not sufficient to provide a long-term perspective on the AMV and finally address its relationship to external forcing or in fact any climate index that describes variability on longer timescales. Therefore, longer timeseries of the AMV are needed. Long AMV timeseries These are typically derived from climate reconstructions based on climate proxies such as tree rings, bivalves or coral skeletons (e.g. Gray et al., 2004; Mann et al., 2008; Svendsen et al., 2014; Wang et al., 2017; Singh et al., 2018). However, these existing This kind of reconstruction is based on statistical models that link the target index with proxy timeseries, using the observational period to calibrate their parameters. The trained models then use the much longer proxy timeseries as input to provide an estimation of the target index in the past.

55 Existing AMV reconstructions disagree on the amplitude and timing of AMV variations variability, especially prior to the beginning of the 18th century (Wang et al., 2017). In addition, many reconstruction methods are known to underestimate the true magnitude of low-frequency variability (Zorita et al., 2003; Esper et al., 2005; Von Storch et al., 2004; Christiansen et al., 2009).

The exact reasons for the disagreement between previous AMV reconstructions are still unclear, but in As a consequence, 60 they also provide conflicting views on the AMV response to external forcing (Knudsen et al., 2014; Wang et al., 2017; Zhang et al., 2019; M Possible reasons for this disagreement are numerous. In general, the reconstructed variability will depend on the predictor data, i.e. the number, types quality and locations of the proxies, as well as on the reconstruction method itself. Obvious differences can be found in the . Previous AMV reconstructions differed in their employed proxy networks , which were either based purely on terrestrial records (Gray et al., 2004; Mann et al., 2008; Wang et al., 2017) or included and types, using 65 only terrestrial or also marine records(Svendsen et al., 2014; Singh et al., 2018). Including . As an example, including marine records seems to be important to correctly capture the AMV in reconstructions (e.g., Saenger et al., 2009; Mette et al., 2021). From the methodological side, limitations of linear methods could play a role. Linear methods might not capture the link between proxies and the target climate index correctly; in this context some non-linear methods have already proved promising (e.g. Hanhijärvi et al., 2013; Michel et al., 2020) yield better reconstructions of AMV variability (e.g., Saenger et al., 2009; Mette et al., 70 2021). Proxy data are only available at a limited number of locations on the globe (see e.g., PAGES2k, 2017), and their availability decreases further back in time. Proxies also contain varying amounts of non-climatic signals, i.e., noise.

As a consequence of the disagreements between the existing AMV reconstructions, their analysis provided conflicting views on the AMV response to external forcing (Knudsen et al., 2014). For instance, a reconstruction of the AMV during the past 12 centuries indicated that the combined contribution of solar and volcanic forcing explain only less than a third of the AMV 75 variance (Wang et al., 2017; Zhang et al., 2019). Another recent study, however, called into question whether external and internal AMV variability could at all be estimated reliably from reconstructions given the uncertainty in both the radiative forcing and the reconstructed AMV indices (Mann et al., 2022) Existing reconstruction methods range from very simple linear methods such as Composite Plus Scaling (Jones and Mann, 2004) or Principal Component Analysis (e.g., Gray et al., 2004), over more complex linear methods such as Bayesian Hierarchical Modelling (Barboza et al., 2014) to non-linear methods such 80 85 Random Forest (Michel et al., 2020), Pairwise Comparison (Hanhijärvi et al., 2013) or Data Assimilation (e.g., Singh et al., 2018). The presence of noise , i.e., non-climatic or mutually unrelated variability , in the statistical predictors may result in biased estimations of parameters of the statistical models such as regression coefficients. This biased estimation in turn leads to a biased amplitude of reconstructed variabilitywhen the predictors are proxy records, or biased estimation of forced variability when the predictor is Especially regression-based methods are known to underestimate the true magnitude of variability, especially on lower frequencies (Zorita et al., 2003; Esper et al., 2005; Von Storch et al., 2004; Christiansen et al., 2009). They also tend to "regress to the mean", i.e. they have difficulties in reconstructing values that lie outside the range of the uncertain external forcing (Zorita et al., 2003; Von Storch et al., 2004; Christiansen et al., 2009)calibration data. This is further exacerbated by the presence of strong warming trends and shortness of the available calibration period (approximately 150 years).

Thus, robust reconstruction methods are needed in order to produce more reliable estimates of the amplitude of the past 90 variability of the AMV in order to better quantify its response to external forcing. This is also a precondition for an unbiased detection of any 'unusual' observed trends and for the subsequent attribution of those trends to a particular forcing, e.g., anthropogenic greenhouse gases. To this end, we need to design reconstruction methods which are more robust against noise and, importantly, do not strongly 'regress to the mean' when the predictors become more noisy or scarce back

in time. As in many disciplines, machine learning methods have successfully gained traction in the climate reconstruction community (e.g., Michel et al., 2020; Zhang et al., 2022; Wegmann and Jaume-Santero, 2023). Here, we explore the potential of the non-linear supervised learning method Gaussian Process Regression (GPR) for climate index reconstructions. GPR finds growing use in climate applications such as climate model emulators (Mansfield et al., 2020) or reconstructions of sea level fields (Kopp et al., 2016) and global mean surface temperature (Büntgen et al., 2021).

Unlike other machine learning methods, such as neural networks, GPR offers greater transparency and is less of a "black box". The number of free parameters is usually much smaller and ideally the parameters have a more direct physical interpretation. A Gaussian Process (GP) describes a distribution over functions with a given mean and covariance structure. The covariance structure is chosen such that the resulting functions best match a given set of observations. This setup appears as more intuitive and closer to the more familiar family of regression methods than convoluted deep learning structures, which in the end may need additional algorithms for their physical interpretation. GPR's non-parametric nature has the advantage that we do not need to make any assumptions about the (non-)linearity of the underlying reconstruction problem. As a Bayesian method, GPR comes with its own uncertainty estimates, which is a very important feature for paleoclimate applications.

We do not only test GPR as a climate index reconstruction tool but also propose a modified input space for the GPR-based reconstructions. To this end, we embed the entire available dataset (proxy data and the target index) in a virtual space. The location of the data timeseries in this space are based on the similarity between the timeseries. The resulting cloud of data points in this virtual space can be viewed as a temporal sequence of images with missing values. The covariance of the GP describes the cross-correlation between the proxy records and the target index across time and virtual space. We use the GPR to fill the missing values, where we do not have observations of the target index. This approach is somewhat similar to kriging in geostatistics, where two-dimensional fields are reconstructed based on point measurements and a known covariance structure. In our case, the input space is not the geographical space but the virtual embedding space and the covariance structure is learned from the data. This set-up has the additional advantage that it can easily accommodate variable proxy availability in time and that the proxy-related uncertainty can be directly accounted for by the parameters of the GP.

To fully judge the methodological performance and related uncertainties, reconstruction methods need to be tested in so-called pseudoproxy experiments (Smerdon, 2012). Many methods have already been tested in such controlled environments, but the evaluation often lacks a thorough assessment of the method's capability to reconstruct the magnitude of the variability on different timescales. In particular, a reconstruction method must be able to capture extreme phases, again to ascertain whether the AMV is sensitive to sudden changes in the external forcing, e.g., after volcanic eruptions, but also to capture possible large internally generated variations, which could occur independent of external forcing.

In this study, we present and test a new method for climate-index reconstructions in order to address the methodological issues outlined above. The method is based on the non-linear supervised learning method Gaussian Process Regression (GPR). As in many disciplines, machine learning methods have started to gain traction in the climate reconstruction community (e.g., Michel et al., 2020). GPR itself finds growing use in climate applications such as climate model emulators (Mansfield et al., 2020) or reconstructions of sea level (Kopp et al., 2016) and global mean surface temperature (Büntgen et al., 2021). We have developed a modified input space for the GPR-based reconstructions, which is designed to adequately handle proxy-related uncertainties

and variable proxy availability in time and to correctly capture the magnitude of multi-decadal variability. We test the method in

130 ~~a~~ Here, we test our proposed framework of the embedded GPR in such a pseudoproxy environment and place special emphasis on the method's skill of reconstructing extreme phases and the magnitude of variability of the AMV.

2 Methods and Data

2.1 Pseudoproxies and simulated AMV index

We generate the pseudoproxies from a simulation of the Common Era (i.e., the past 2000 years) with the Max Planck Institute

135 Earth System Model (MPI-ESM). The model version corresponds to the MPI-ESM-P LR setup used in the 5th phase of the Coupled Model Intercomparison Project (CMIP5, Giorgetta et al., 2013). A detailed description of the simulation can be found in Zhang et al. (2022). The target of the pseudo-reconstructions is the simulated AMV index (AMVI). We define the AMVI as the spatial mean of annually averaged sea surface temperature anomalies (SST) in the North Atlantic (0 to 70°N and 80°W to 0°E). The SST anomalies are calculated against the mean over the entire simulation period. We do not further detrend the 140 AMVI because it is difficult to define a meaningful trend period in the paleo context. In the case of real reconstructions, all proxies and the AMVI would be available for overlapping periods with different length, and it is not possible to define a meaningful common trend ~~which that~~ could be subtracted from all records.

The pseudoproxies are defined as timeseries of the simulated ~~surface air~~ temperature at the model grid points closest to existing proxy sites in the PAGES2k database (PAGES2k, 2017). Over land, we use 2m annual mean air temperature, over

145 ocean we use annual mean sea surface temperature. We do not use all available proxy sites from the PAGESk data base but only ~~a~~ subset thereof. We limit our selection of proxy sites to those within the North Atlantic domain (10 to 90°N and 100°W to 30°E) with ~~a temporal resolution of five years or higher annual resolution or finer~~. Out of these, we further select only those locations at which the pseudoproxies have a correlation of 0.35 or higher with the AMVI during the last 150 simulation years (in this case, both the AMVI and the pseudoproxies are detrended before calculating the correlation). The final proxy network 150 consists of 23 pseudoproxies (Fig.1a).

We ~~test the embedded Gaussian Process Regression (emGP) in three test cases~~ design three sets of pseudoproxies to account for different sources of uncertainty: In the first test case (TCpp), we use perfect pseudoproxies, i.e., the pseudoproxies contain only the temperature signal. In the second test case (TCnpp), we use noisy pseudoproxies, i.e., the pseudoproxies contain additional non-climatic noise. The non-climatic noise is generated by adding white noise to the perfect pseudoproxies. The 155 amplitude of the white noise is defined such that the correlation between the noisy and the perfect pseudoproxies is 0.5; i.e., the amplitude of the white noise corresponds to the standard deviation of the perfect pseudoproxy times $\sqrt{3}$. This is a reasonable choice, as the correlation for real proxies with observations ranges from 0.3 to 0.7. The amount of white noise applied here is also well within the range of other pseudoproxy studies (e.g., Smerdon, 2012). To ensure that the performance with noisy data is independent of the specific noise realisation, we create an ensemble of 30 noise realisations. In both TCpp and TCnpp

160 we assume that all records are available at every point in time, i.e., that the network size remains constant in time. In reality, different proxy records cover different periods and the network size is not constant (Fig.1b). Therefore, we set up a third test

case (TCp2k) with realistic temporal proxy availability from the PAGES2k database and both perfect and noisy pseudoproxies.

In all three test cases, the pseudoproxy records have annual resolution. The reconstruction period corresponds to the last 500 simulation years for TCppp and TCnpp, and to the entire 2000 simulation years for TCp2k.

165 To test the sensitivity of the method to the underlying climate-model simulation, we repeat the test cases TCppp and TCnpp with an analogously derived set of 25 pseudoproxies and AMVI from simulations with the Community Climate System Model (CCSM4, Gent et al., 2011). We combine the 'past1000' simulation (Landrum et al., 2013; Otto-Bliesner, 2014) and one 'historical' simulation (Gent et al., 2011; Meehl, 2014) from the CMIP5 suite and use the last 500 years of the combined data set. From the historical simulations, we used the ensemble member r1i1p1. The results are displayed in Appendix B.

170 2.2 Benchmark reconstruction

To have a benchmark for the GPR-based reconstruction in the cases TCppp and TCnpp, we use pseudo-reconstructions with a multi-linear Principal Component Regression (PCR). PCR is well established as a climate-index reconstruction method and has been used e.g., for reconstructions of the global mean surface temperature (PAGES2k, 2019) and the AMVI (Gray et al., 2004; Wang et al., 2015). The selected proxy timeseries are first decomposed into principal components (PCs); the latter are then used as predictors in a linear least-squares regression to obtain the AMVI for those timesteps where proxies and AMVI overlap. In other words, the AMVI is expressed as a function of PCs of the original proxies (Eq. 1). We do not use all PCs but only retain those with a cumulative explained variance of 99.5%. The trained model can then be used to reconstruct the AMVI for timesteps where we have only proxies available.

$$AMVI(t) = f_{PCR}(PC_1(t), \dots, PC_n(t)) \quad (1)$$

180 2.3 Gaussian Process Regression

2.3.1 The Concept

Gaussian Process Regression (GPR) is a Bayesian, non-parametric, supervised learning method (Rasmussen and Williams, 2006). Just like a probability distribution describes random variables, a Gaussian Process (GP) describes a distribution over functions with certain properties. A GP is ~~described~~ determined by a mean function and a covariance function.

$$185 \quad f(\mathbf{x}) \sim GP(\mu(\mathbf{x}), k(\mathbf{x}, \mathbf{x}')) \quad (2)$$

The mean function $\mu(\mathbf{x})$ describes the mean of all functions within the GP at location \mathbf{x} . In the absence of other knowledge, it is typically assumed that the mean of all functions within the prior GP is zero everywhere. The covariance function $k(\mathbf{x}, \mathbf{x}')$ describes the statistical dependence between the function values at two different points in the input space. The exact covariance structure is ~~defined~~ prescribed by a kernel function. Kernel functions range from very simple (e.g. linear, radial basis functions) to ~~very~~ more complex (e.g., Matern functions, periodic). In principle, there is no limit to the kernel complexity and finding

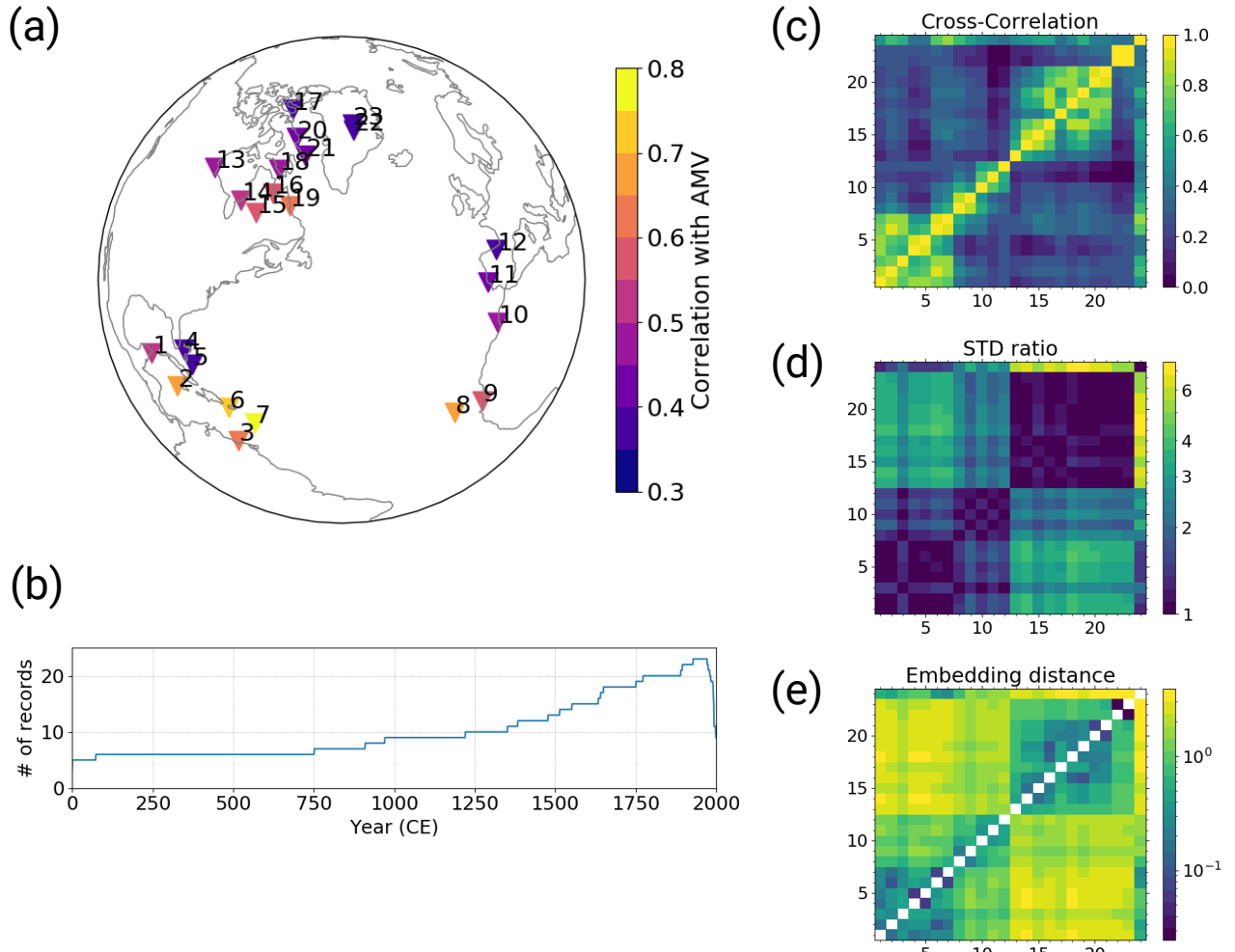


Figure 1. The selected pseudoproxy records and resulting distance metrics based on the MPIESM simulation. **(a)** the locations of the records, colour-coded with the correlation between the records and the AMVI during the last 150 simulation years (after detrending); **(b)** the number of available proxy records at the selected locations within the PAGES2k dataset over time; **(c)** cross-correlation; **(d)** standard deviation ratio and **(e)** the resulting embedding distances from the combination of both. Matrix indexes 1 to 23 are the selected pseudo proxy records as [labeled](#) in (a), index 24 is the simulated AMVI. The diagonal entries in (e) are left empty because zero cannot be displayed on the logarithmic [colour](#) scale.

the right kernel can be considered an art in itself (e.g. Duvenaud et al., 2013). Once a general functional form of the kernel has been chosen (e.g. radial basis function), the specific form is determined by the kernel ~~hyperparameters~~parameters. Since the underlying GP model itself is non-parametric, kernel parameters are often also referred to as hyperparameters (Rasmussen and Williams, 2006). These hyperparameters are either prescribed ~~apriori~~a priori if they are known, or learned 195 from the data through optimisation ~~if they are unknown~~ (e.g. ~~through~~ maximum likelihood estimation) ~~if they are unknown~~. Based on the so-determined kernel, a covariance matrix is created by evaluating the kernel function for all pairs of available observations in the training data.~

Without being constrained by data, the prior GP is a distribution of all functions with the given mean and covariance (Eq. 2). In order to use the GP for regression and prediction, the prior GP is combined with the additional information from the training 200 data through Bayes theorem (Rasmussen and Williams, 2006). Thus, the posterior GP is obtained, conditional on the data. Predictions at unseen input points can then be made by calculating the joint posterior distribution conditional on the training data and the unseen input points (see Appendix A and Rasmussen and Williams (2006) for a more detailed description).

In the simplest way of using GPR for AMV reconstructions, analogous to classical climate-index reconstruction methods, the AMVI would be the target function $f(\mathbf{x})$ and the proxy data the input data \mathbf{x} . Once a suitable kernel is selected, its 205 hyperparameters are estimated through training with the available values of \mathbf{x} and $f(\mathbf{x})$. With the trained GP model, the probability distribution of the AMVI for past times can be estimated conditioned on the proxy data \mathbf{x} for these past times.

One known drawback of GPs is the bad scaling behaviour of the computing time required to estimate the hyperparameters with respect to the number of available observations, also called batch size. The training time of a GP scales with n^3 , where 210 n is the batch size. This is mainly due to the necessity to invert the covariance matrix (e.g., Rasmussen and Williams, 2006). Regression problems with more than 1000–10000 observations become difficult to handle with the original GP formulation (hereafter full GP) due to time and computing memory limitations. Even though paleo data sets are not what we would typically call *Big Data*, they can already become challenging for GPs if the reconstruction period spans thousand years or more.

Various GP variants have been proposed to overcome this limitation (e.g., Särkkä, 2013; Hensman et al., 2013). One variant 215 is the so-called *stochastic variational GP* (SVGP, Hensman et al., 2013). The SVGP combines stochastic gradient descent (i.e., training with minibatches), variational inference (Thus, the posterior GP is obtained, i.e. inference through optimisation) and a low-rank approximation of the covariance matrix based on so-called inducing points. Put simply, the inducing points are a small subset of the original dataset that represents the properties of the complete dataset. In other words, the true GP posterior is approximated by a GP that is conditioned on the inducing points. The location of the inducing points in input space can 220 either be prescribed manually (e.g. randomly) or they can be optimised along with the kernel hyperparameters. The training time of the SVGP scales with m^3 , where m is the number of inducing points (Hensman et al., 2013), only those functions are selected that agree with the training data in a given uncertainty range. Predictions at previously unseen input points are then given by that posterior distribution of functions evaluated at those unseen input points.

We test the suitability of both the full GP as well as the SVGP (hereafter sparse GP) for climate-index reconstructions. Our 225 scripts are based on the python package GPflow (Matthews et al., 2017). The hyperparameters are learned through optimisation

with the Adam Optimiser (Kingma and Ba, 2014), which is provided with GPflow. For the full GP, we repeat the optimisation step 1000 times. For the sparse GP, we initialise the inducing points as every tenth point in time and the optimise the locations along with the hyperparameters. We use minibatches with a size of 2000 and repeat the optimisation step 4000 times. The respective number of optimisation steps is sufficient for the estimated likelihood to reach an equilibrium.

230 2.3.2 Embedding Space

As described above,

2.3.2 Finding the right regression space

As described for the PCR, classical climate-index reconstruction methods formulate their underlying statistical model ~~in a way~~ ~~so~~ that the climate index is assumed to be a function of temperature, the proxy values or e.g. principal components thereof.

235 In other words, the regression is performed in temperature/proxy/PC space; the proxies/PCs are the predictors and the climate index is the predictand. ~~Initially, we tested the GPR in~~ ~~If we reconstruct the AMVI with GPR in this classical setup, the target AMVI becomes the posterior mean function and the covariance is estimated across the proxy space. In this setup, the GP~~ ~~With the trained GP model, the AMVI can be reconstructed by evaluating the GP at the proxy values that occurred during the reconstruction period.~~ Fig. 2a shows a schematic for the regression in proxy space for an example where the AMVI is given as 240 a function of two pseudoproxy records p_1 and p_2 . In this example, the posterior mean AMVI-function forms a surface in the space spanned by p_1 and p_2 . Note that in our pseudoproxy experiments we use 23 pseudoproxies (Fig. 1a), so the proxy space is actually 23-dimensional, which is impossible to visualise.

245 In initial tests, the GPR reconstruction in proxy space did not perform better than the PCR; the underestimation of variability was as strong as with the PCR well; the variability of the AMVI was strongly underestimated (not shown). One A possible explanation is that GPs ~~cannot extrapolate well to ranges unseen during training. In~~ are very good interpolators but bad at extrapolating to regions of the ~~input space where available predictors are sparse~~, the GP proxy space that have not been sampled during training (e.g. upper left and lower right quadrants in the example of Fig. 2a) or where predictors become sparse (lower left quadrant in Fig. 2a). In those cases, the GPR estimation will fall back to the prior mean function (regression to the mean). ~~Instead they are very good interpolators. In order to make use of this, we tried to~~ and the predictive skill becomes very small. From a mathematical point of view, this setup of the regression in proxy space is also actually not suitable for GPR. Real-world proxies come with large uncertainties, and while GPs are designed to handle uncertain targets, they assume that the inputs are without uncertainty. Therefore, we approach the problem differently and set up the ~~GP in a modified input space~~, which we denote here as embedding space. We will refer to this setup as embedded GPR (emGPR) ~~GPR in a way that leverages~~ two GPR strengths: (1) being good interpolators and (2) handling uncertain targets.

255 We

In our new approach, we embed the entire available data set (the selected ~~proxy~~ ~~pseudoproxy~~ records and AMVI at all points in time where observations are available) in a virtual space. ~~Time is considered as an additional dimension of the embedding space. Each timeseries is assigned a constant location in this virtual space so that the positions of the~~ The cloud

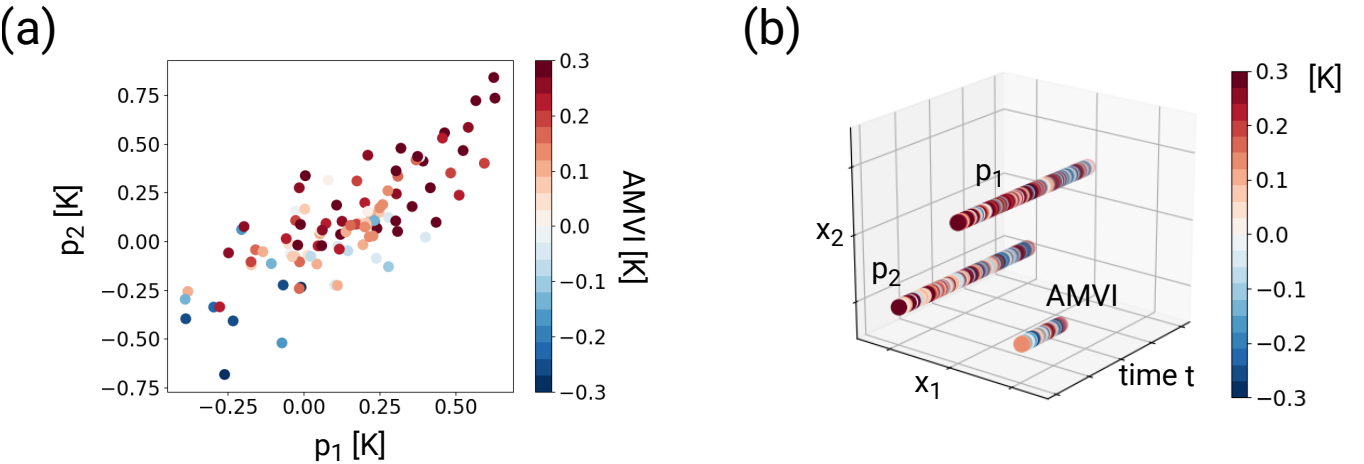


Figure 2. Schematic visualisation of the regression spaces for an example with two proxy records p_1 and p_2 and the AMVI. (a) GPR in proxy space: The independent variables are the temperature anomalies of the proxy records; the dependent variable is the AMVI (colour-coded) (b) GPR in the embedding space: the independent variables are the locations in the embedding space and time, the dependent variables are the temperature anomalies of the proxy records and the AMVI (colour-coded). In this simplified example, the three timeseries are located such that the distance between them is equal for all respective pairs of records.

of data points can be viewed as a sequence of images in this virtual space. The images contain missing values at timesteps where we do not have AMVI observations available. The climate-index reconstruction problem thus becomes similar to an image-reconstruction problem. The GPR reconstructs the AMVI by filling the missing values based on the surrounding proxy values. In this framework, the GPR inputs are the locations in the embedding space and the GPR targets are the temperature anomalies of the proxies and the AMVI:

$$\Delta T_i = f_{GPR}(t, \mathbf{x}_i), \quad (3)$$

where ΔT_i is either a proxy record p_i or the AMVI, and \mathbf{x}_i is the location of the respective record within the embedding space. Fig. 2b shows a schematic view of this embedding space for the example with two pseudoproxies and the AMVI. The location of each timeseries within the embedding space is constant, so that the temporal sequence of data of one particular proxy series forms a straight line parallel to the time axis. The location of each record is based on its similarity to all other records. The more similar two records are, the closer they are located in the embedding space. To adequately reflect the distances between the proxy records and the AMVI, the embedding space needs to have a dimension of $(q-1) + t(q-1)$, where q is the number of proxy timeseries including the AMVI timeseries and $t = 1$ for the time dimension. This is easiest to understand if one imagines the case where all timeseries have the same distance from each other (as shown in Fig. 2b). To arrange, e.g. three timeseries with equal distances from each other, one needs a two-dimensional space (spanned by x_1 and x_2 in Fig. 2b). In case of the MPIESM-based proxy network, the embedding space has thus 24-23 dimensions (23 proxy records, 1

275 AMVI). With time as an additional dimension, the resulting space has a total of 24 dimensions. In the following, we will use \mathbf{r} to refer to a point in space and time, and \mathbf{x} and t to refer to points in space and time, and \mathbf{x} and t to refer to points in space and time, respectively.

The prescribed distance between the virtual locations \mathbf{x}_i reflects the similarity between the respective timeseries, e.g. the similarity between a proxy record and the AMVI, or the similarity between two proxy records. We then use the GP to fit find a function that fits the entire dataset in this virtual space and to interpolate the AMVI at the virtual locations \mathbf{x}_{AMV} for points in time where we do not have observations. By performing the regression/interpolation in the embedding space, the coordinates of the embedding space become the predictors/inputs and both the proxies and the climate index become the predictands/targets. This allows for a much bigger training data set and increases the range of climate variability seen during training. Because time is an additional dimension, and the kernel is also a function of time separation, this approach also takes temporal auto-correlation and With the right kernel formulation (see Sect. 2.3.4), we can account not only for cross-correlations 280 between the different timeseries into account.

In the interpolation process, a, but also for temporal auto-correlation: A data point in the embedding space at time t_m is affected by all other surrounding points in the embedding space at time t_m and to a smaller extent also at times $t_n > t_m$ and $t_k < t_m$. The degree of influence is determined by the distance between the points in the embedding space and the typical length- and timescale of the kernel function. The closer two points are, the larger the their influence.

290 Thus, the AMVI is still reconstructed based on the information from the pseudoproxies, but we have formulated the problem such that the GP can handle the proxy-related uncertainty correctly, because the pseudoproxies are now targets and no longer inputs. An additional advantage is that we can use this setup with variable proxy availability in time without having to retrain the model each time the proxy availability changes. Instead, the "images" simply have more missing values as the number of proxies decreases further back in time.

295 2.3.3 Defining the distance matrix

Finding the right position \mathbf{x} for each proxy record and the target index in the embedding space is an important and non-trivial step. Since we care only about the relative distance in the embedding space and not the absolute location, we can specify the distance between each pair of q records (proxies and AMVI) in a distance matrix \mathbf{D} and determine the coordinates via multi-dimensional scaling . The problem then reduces to specifying the distance matrix. (MDS, e.g., Mead, 1992). MDS uses 300 the information of dissimilarity between objects to place these objects in a Cartesian space of a given dimension, such that the distance between the objects in the new space reflects the dissimilarity in an optimal way. In our case, the objects are the proxy records and the AMVI, and the given dimension is 23.

2.3.4 Defining the distance matrix

We define the distance matrix based on an appropriate distance metric. This metric could in principle be any distance metric 305 such as the Euclidian distance or similar. To be used as a distance metric in MDS, a metric must meet the following three criteria: it needs to be (1) positive, (2) zero, when it is applied on the object with itself and (3) symmetric (e.g., Mead, 1992).

We chose to define the distance based on the ~~cross-correlation~~-cross-correlation (CC, Fig. 1c) and the standard deviation ratio (SR, Fig. 1d) of the respective records. The SR of two timeseries p_i and p_j is defined as

$$SR_{ij} = \begin{cases} \frac{std(p_i)}{std(p_j)}, & \text{if } std(p_i) > std(p_j) \\ \frac{std(p_j)}{std(p_i)}, & \text{if } std(p_i) < std(p_j), \end{cases} \quad (4)$$

310 this way, the SR is symmetric, fulfilling the third criterion for the distance metric. Assuming that the records are all positively correlated, the distance measure between two timeseries p_i and p_j is defined as

$$D_{ij} = (1 - CC_{ij}) * SR_{ij}, \quad (5)$$

i.e., the distance will be small when the CC is high and the records have similar amplitudes of variability, and larger when the CC is low and/or the records have very different amplitudes of variability (Fig. 1e). This choice of distance metric 315 outperforms equidistant coordinates and a metric based solely on CC (not shown). The SR of two timeseries p_i and p_j is defined as With equidistant coordinates all records determine the AMVI to the same degree, regardless of their actual similarity to the AMVI. With a metric based solely on CC, the reconstruction is dominated by records with high variability and the resulting AMVI variability is overestimated. The additional SR-scaling yields improved variability estimates.

$$RA_{ij} = \begin{cases} \frac{std(p_i)}{std(p_j)}, & \text{if } std(p_i) > std(p_j) \\ \frac{std(p_j)}{std(p_i)}, & \text{if } std(p_i) < std(p_j), \end{cases}$$

320 this way, the SR is symmetric – a necessary condition for a distance measure. The so determined unitless distances in the embedding space range from The final distance matrix D is then obtained by evaluating Eq. 5 for all pairs of records. For all pairs of pseudoproxies, the distance is estimated from the entire simulation length. For calculating the distance between the AMVI and the pseudoproxies, we use only the last 150 years (years 1850 to 2000) and linearly detrend both AMVI and pseudoproxies before the calculation. The so determined unitless distances range from 0.02 to 3.91 for the MPIESM-based 325 network (Fig. 1e).

The distance matrix is then transformed into coordinates of a $(q-1)$ -dimensional space via multi-dimensional scaling. Time becomes an additional dimension of this new space, and the determined coordinates for each record are constant in time. The distance between the time steps is normalised to be of the same order of magnitude as the distances between the records. We rescale the time axis so that the distance between time steps equals the mean of the distance matrix D . In the case of the 330 MPIESM-based network (Fig. 1), the mean of the distance matrix is 1.44. For the CCSM-based network (Fig. B1), the mean of the 1.10. The resulting distance matrix is 1.10.

then used as input for the MDS algorithm to obtain the coordinates in a 23-dimensional space. The embedding distance reflects the actual geographical distance to a certain degree. Records that are close in actual space tend to be close also in the embedding space, as they have higher cross-correlations and similar standard deviations (Fig. 1e).

335 2.3.4 Kernel Design and Hyperparameters

We choose a very simple kernel function, the radial basis function (RBF), because we have no prior information that would justify the use of a more complex kernel. Complex kernels would introduce additional uncertainty and reduce the interpretability of the results. We define the kernel k as an additive kernel of two RBF components, $k = k1 + k2$:

$$340 \quad k1(t_i, t_j) = \sigma_{f,t}^2 \exp\left(\frac{1}{2} \left(\frac{|t_i - t_j|}{l_{f,t}}\right)^2\right) \quad (6)$$

$$k2(\mathbf{r}_i, \mathbf{r}_j) = \sigma_{f,r}^2 \exp\left(\frac{1}{2} \left(\frac{|\mathbf{r}_i - \mathbf{r}_j|}{l_{f,r}}\right)^2\right). \quad (7)$$

where The final kernel or covariance equation is then given as

$$k = k1 + k2 \quad (8)$$

In Eq. 6 and 7, $|*$ is the Euclidian distance between two points t_i and t_j or \mathbf{r}_i and \mathbf{r}_j . The l_f and σ_f^2 are the hyperparameters of the respective kernels. l_f denotes a typical lengthscale of the target function, while σ_f^2 describes the signal variance, e.g., a function with small l_f and large σ_f^2 will be very wiggly. A third additional hyperparameter σ_n^2 denotes the likelihood or noise variancee (see also Appendix A). If σ_n^2 is small, the fitted function will be very strongly constrained by the training data. If σ_n^2 is larger, the fitted function is less constrained by the training data and more robust against overfitting.

The first kernel $k1$ operates on the time dimension only, i.e. it controls how much the neighbouring time steps at one embedding location influence the value at time t_j . This could be considered as a mean typical timescale of variability in the dataset. The second kernel $k2$ operates on all dimensions of the embedding space, including the time dimension. This enables interaction between locations at time t_j and neighbouring time steps. This kernel setup outperforms a kernel that consisted only of $k2$ and one where $k2$ did not include the time dimension (not shown). The higher skill of this kernel makes sense if one considers how the kernel design affects the interactions between the different timeseries. Having only $k2$ does not consider that the timescale of auto-correlation may not be the same as the timescale of cross-correlation. It, therefore, makes sense to have $k1$ operate across the time dimension only. If $k2$ operated only across the embedding dimensions, no interaction between different records across time would be possible.

Because $k2$ operates on both the time and the embedding dimensions, we rescale the time steps to be of the same order of magnitude as the distances between the records. This is necessary to allow for the interaction across records and time. Otherwise, the length scale of $k2$ would either be dominated by the time step or by the embedding distance. One rescaled time

step equals the mean of the distance matrix \mathbf{D} . In the case of the MPIESM-based network (Fig. 1), the mean of the distance matrix is 1.44. For the CCSM-based network (Fig. B1), the mean of the distance matrix is 1.10.

A third additional hyperparameter σ_n^2 denotes the likelihood or noise variance (see also Appendix A). The noise variance enables the GPR to handle target uncertainty. A small σ_n^2 indicates that the targets have low uncertainty and the fitted function will be very strongly constrained by the training data. If σ_n^2 is larger, the targets come with large uncertainty. The fitted function is then less constrained by the training data and more robust against overfitting. Introducing σ_n^2 is similar to the so-called nugget effect in geostatistics. The noise variance σ_n^2 is assumed to be the same across all dimensions, i.e., the learned estimate will be the same for all pseudoproxies and the AMVI. This is a simplification, because every pseudoproxy contains its own level of noise. We will show that this simplification is a good first approximation and enables the GPR to handle uncertain pseudoproxies well.

2.3.5 GP scaling behaviour

One known drawback of GPs is a bad scaling behaviour of the computing time required to estimate the hyperparameters with respect to the number of available observations, also called batch size. The training time of a GP scales with n^3 , where n is the batch size. This is mainly due to the necessity to invert the covariance matrix (e.g., Rasmussen and Williams, 2006). Regression problems with more than 1000-10000 observations become difficult to handle with the original GP formulation (hereafter full GP) due to time and computing memory limitations. Even though paleo data sets are not what we would typically call *Big Data*, they can already become challenging for GPs if the reconstruction period spans thousand years or more.

Various GP variants have been proposed to overcome this limitation (e.g., Särkkä, 2013; Hensman et al., 2013). One variant is the so-called *stochastic variational GP* (SVGP, Hensman et al., 2013). The SVGP combines stochastic gradient descent (i.e., training with minibatches), variational inference (i.e., inference through optimisation) and a low-rank approximation of the covariance matrix based on so-called inducing points. Simply put, the inducing points are a small subset of the original dataset that represents the properties of the complete dataset. In other words, the true GP posterior is approximated by a GP that is conditioned on the inducing points. The location of the inducing points in input space can either be prescribed manually (e.g. randomly) or they can be optimised along with the kernel hyperparameters. The training time of the SVGP scales with m^3 , where m is the number of inducing points (Hensman et al., 2013). Here, we test both the full GP and the SVGP for climate-index reconstruction in the embedding space. In the following, we will refer to the full embedded GP as full emGP and the embedded SVGP as sparse emGP.

2.3.6 Technical notes

Our scripts are based on the python package GPflow (Matthews et al., 2017). The hyperparameters are learned through optimisation with the Adam Optimiser, which is a stochastic gradient descent algorithm widely used in machine learning applications (Kingma and Ba, 2014). We use the algorithm as provided by GPflow. For the full GP, we repeat the optimisation step 1000 times. For the sparse GP, we initialise the inducing points as every tenth point in time and the optimise the locations along

with the hyperparameters. We use minibatches with a size of 2000 and repeat the optimisation step 4000 times. The respective number of optimisation steps is sufficient for the estimated likelihood of reaching an equilibrium.

395 2.4 Training and Testing

In the real world, SST measurements are only available since approximately 1850. Therefore, AMV observations are also only available from 1850 to today. We use this criterion to divide our pseudo-data set into training and testing data. The relationship between the pseudoproxies and the simulated AMVI can be inferred only from the last 150 years of the simulation, the remaining years of the simulated AMVI are used for testing. This may not be the most effective way of splitting a data set 400 in the machine-learning context, but it best reflects the actual data availability in the paleo-context.

405 For the emGPR reconstructions, the training input data consists of the time steps t_j and the embedding coordinates \mathbf{x}_i of the benchmark PCR reconstruction, which takes place in PCR-space, the training inputs are the most recent 150 years of the retained principal components and the training targets are the corresponding 150 years of simulated AMVI (i.e. years 1850 to 2000). In the testing period, the AMVI is reconstructed with the trained regression model and the remaining 350 years of the retained principal components as inputs.

410 For the emGPR reconstructions, the training inputs are the locations \mathbf{r}_i of the pseudoproxies and the AMVI. For the pseudoproxies, all time steps are used for training (i.e. years 1500 to 2000); for the AMVI only the time steps corresponding to the last 150 simulation years are used for training (i.e. the years 1850 to 2000 (left matrix in Eq. ??)). The training target data is thus the entire available data set, i.e., the targets are the corresponding values of the 23 proxy records p_i over the full 500 years and the AMVI record over the last 150 years (right matrix in Eq. ??). During testing, the AMVI is . During training, the kernel hyperparameters and the noise variance are learned. The AMVI is then reconstructed by evaluating the trained emGP at the embedding location of the AMVI $\mathbf{x}_{AMV} = \mathbf{x}_{24}$ and the timesteps corresponding to the remaining 350 simulation years (Eq. ??).-

$$\left[\begin{array}{cccc} t_1 & x_{1,1} & \dots & x_{1,23} \\ \vdots & \vdots & \ddots & \vdots \\ t_m & x_{1,1} & \dots & x_{1,23} \\ \vdots & \vdots & & \vdots \\ t_1 & x_{23,1} & \dots & x_{23,23} \\ \vdots & \vdots & \ddots & \vdots \\ t_m & x_{23,1} & \dots & x_{23,23} \\ t_{m-150} & x_{24,1} & \dots & x_{24,23} \\ \vdots & \vdots & \ddots & \vdots \\ t_m & x_{24,1} & \dots & x_{24,23} \end{array} \right] \left[\begin{array}{c} p_1(t_1) \\ \vdots \\ p_1(t_m) \\ p_{23}(t_1) \\ \vdots \\ p_{23}(t_m) \\ \vdots \\ AMVI(t_{m-150}) \\ \vdots \\ AMVI(t_m) \end{array} \right]$$

415

$$\begin{bmatrix} t_1 & x_{24,1} & \dots & x_{24,23} \\ \vdots & \vdots & \ddots & \vdots \\ t_{m-151} & x_{24,1} & \dots & x_{24,23} \end{bmatrix} \begin{bmatrix} AMV(t_1) \\ \vdots \\ AMV(t_{m-151}) \end{bmatrix},$$

where t_1 is the simulated year 1500, and t_m the simulated year 2000.

2.5 Principle Component Regression

To have a benchmark for the emGPR reconstruction in the cases TCppp and TCnpp, we use pseudo-reconstructions with a multi-linear Principle Component Regression (PCR). PCR is well-established as a climate-index reconstruction method and has

420 been used e.g., for reconstructions of the global mean surface temperature (PAGES2k, 2019) and the AMVI (Gray et al., 2004; Wang et al., 2019). For the PCR, the AMVI is expressed as a function of principal components of the original pseudoproxies. The selected proxy timeseries are first decomposed into principal components; the latter are then used as predictors in a linear least-squares regression to obtain the AMVI. We do not use all principal components but only the first q with a cumulative explained variance of 99.5%.

425 The PCR does not make use of the embedding space. In case of the PCR, the training inputs are the most recent 150 years of additional advantage that the training set is much bigger than in the q -selected principal components and the training target is the corresponding simulated AMVI (Eq. ??). In the testing period, the AMVI is reconstructed with the trained regression model with the remaining 350 years of the selected q principal components as inputs (Eq. ??). classical setup. Thus, we increase the range of climate variability seen during training and reduce the risk of reconstructing climate states that the

430 model has not been trained with.

$$\begin{bmatrix} pc_1(t_{m-150}) & \dots & pc_q(t_{m-150}) \\ \vdots & \ddots & \vdots \\ pc_1(t_m) & \dots & pc_q(t_m) \end{bmatrix} \begin{bmatrix} AMV(t_{m-150}) \\ \vdots \\ AMV(t_m) \end{bmatrix}$$

$$\begin{bmatrix} pc_1(t_1) & \dots & pc_q(t_1) \\ \vdots & \ddots & \vdots \\ pc_1(t_{m-151}) & \dots & pc_q(t_{m-151}) \end{bmatrix} \begin{bmatrix} AMVI(t_1) \\ \vdots \\ AMVI(t_{m-151}) \end{bmatrix}$$

3 Pseudo-reconstructions

3.1 TCppp: Perfect pseudoproxies

435 With perfect pseudoproxies, the best overall reconstruction is achieved by the full emGPR. The reconstructed AMVI closely follows the target AMVI except for the period from approximately 1630 to 1680 (Fig. 3a). This is reflected by the high correlation with the target AMVI (0.93 for the smoothed index). There is a weak negative mean bias, corresponding to 20% of the target standard deviation, which stems mainly from the ~~50-year 50-year~~ period from 1630 to 1680. ~~As expected, the~~
440 ~~The~~ GP related uncertainty, as given by the 95th percentile of the posterior distribution, is small for the years 1850 to 2000 where the AMVI has been constrained during training. The uncertainty increases for the reconstruction period. Overall, the
posterior uncertainty estimate appears a bit too large - i.e., too conservative - because the true AMVI always lies within the
95% confidence interval. The full emGPR captures the magnitude of variability very well, ~~the~~ The standard deviation ratio of 0.93 indicates only a small underestimation of 7%. Also, the period of very low AMVI following several volcanic eruptions between 1800 and 1850 is well captured, the reconstructed and target AMVI are almost indistinguishable. The spectrum of
445 the reconstructed AMVI agrees well with the spectrum of the target AMVI; the full emGPR captures the variability at all frequencies (Fig. 3b).

The sparse emGPR captures the main features of the target AMVI, but the reconstruction is less accurate (Fig. 3c). The correlation is lower (0.79 for the smoothed index), and there are more periods with larger deviations between the reconstruction and the target. Interestingly, the sparse emGPR has large mismatches during ~~other different~~ periods than the full emGPR. The
450 full emGPR has the largest mismatch in the years 1630 to 1680, the sparse emGPR has the largest mismatches in the years 1720 to 1830. The mismatches result in a positive mean bias corresponding to 33% of the target standard deviation. The GP related uncertainty is the same as the uncertainty from the full emGPR, but in the sparse case, the uncertainty is approximately constant over the entire period. The standard deviation ratio is 0.80, i.e., the variability is underestimated by 20%. This is, e.g. visible for the years 1800 to 1850, where the very low AMVI is not captured as well as by the full emGPR. The spectrum of
455 the reconstruction still agrees well with the target spectrum, but there is a slight overestimation of variability at the very high frequencies and an underestimation at lower frequencies at timescales of 80 to 100 years (Fig. 3d). Differences in the skill of the full and sparse emGP might partly be explained by different estimates of hyperparameters (see left halves of Fig. 5).
We assume that the hyperparameters learned with the full emGPR are closer to the truth. Both the estimated timescale of auto-correlation ($l_{f,t}$) and the signal variance ($\sigma_{f,t}$ and $\sigma_{f,r}$) are underestimated by the sparse emGP.

460 The PCR reconstruction achieves the highest correlation (0.95 for the smoothed index) and comes with the smallest uncertainty range, but at the cost of a larger underestimation of variability and a systematic bias towards higher AMVI values, for periods during which the AMVI is outside of the range of the training period (Fig. 3e). This is especially apparent during the period of the very low AMVI from 1800 to 1850, where the target AMVI lies outside of the PCR uncertainty range. The mean bias corresponds to 79% of the target standard deviation. The standard deviation ratio of 0.65 indicates an underestimation of the variability by 35%. The underestimation occurs systematically at lower frequencies in the multi-decadal range; the high-frequency variability (timescales shorter than 30 years) is well captured (Fig. 3e).

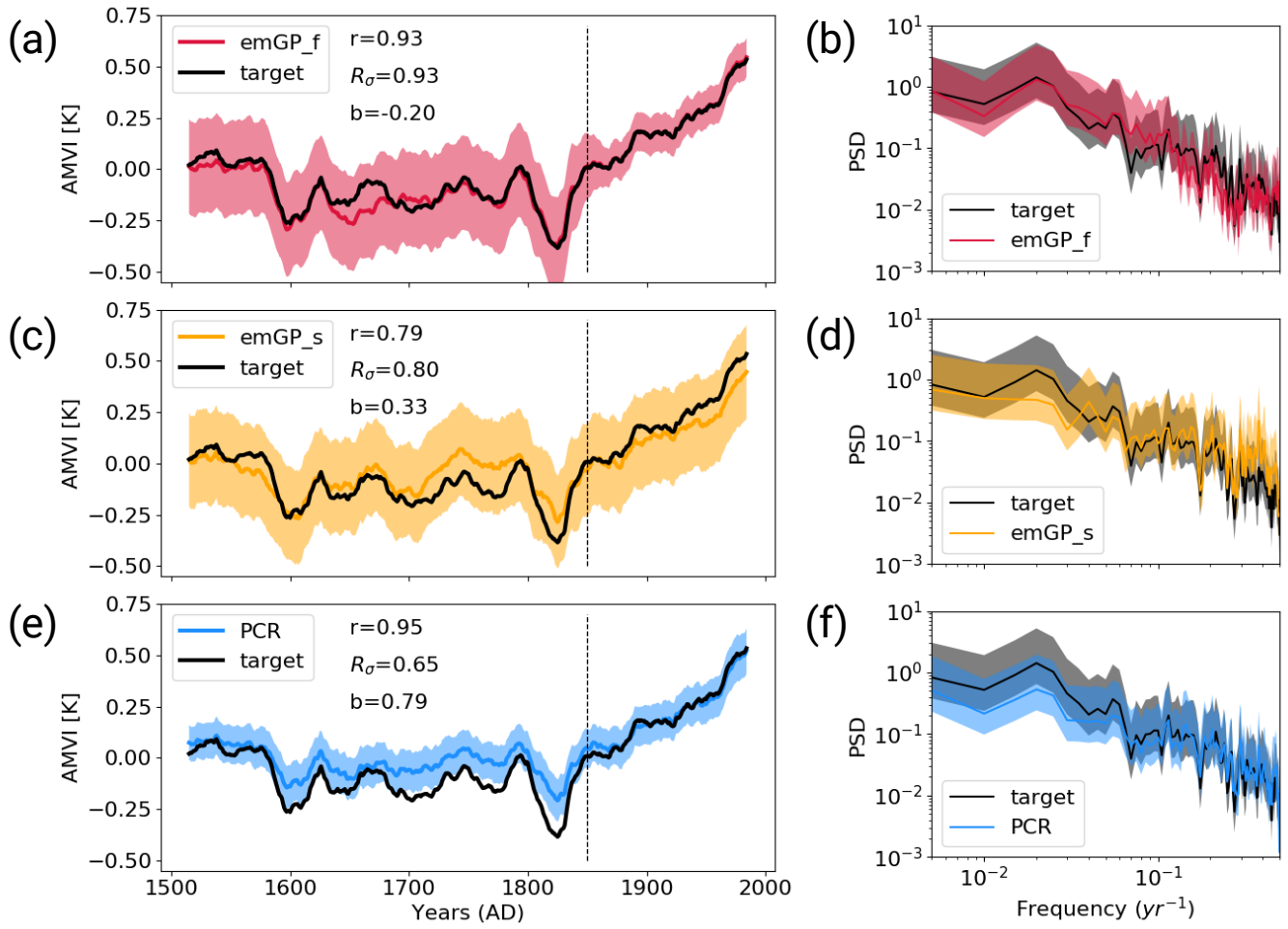


Figure 3. Reconstructions with perfect MPIESM-pseudoproxies based on (a,b) the full emGPR, (c,d) the sparse emGPR and (e,f) PCR. Left-hand panels show the smoothed reconstructed and target timeseries. The dashed line marks the separation between training and testing periods. Shading indicates the 95% confidence interval (CI). The CI is determined by the posterior GP distribution for the full and sparse emGP. For the PCR, the CI is derived from the uncertainty in the regression coefficients, which is based on the t-distribution. The metrics r , R_σ and b denote correlation, the ratio of standard deviations and the bias relative to the target standard deviation, respectively. Subscripts *sm* and *yr* denote smoothed and unsmoothed data, respectively. The metrics are calculated for the smoothed timeseries over the reconstruction period (1500 to 1850). Right-hand panels show the Welch powerspectra power spectra of the target and reconstructed AMVI. Shading indicates the 95% confidence interval as obtained from the χ^2 -distribution. The power spectral density (PSD) is given in $\text{K}^2 \text{ yr}$.

With CCSM4-based pseudo proxies, the results for the full and sparse emGPR are consistent with the MPIESM-based reconstructions (cf. Fig. 3a-d and Fig. B2a-d). The PCR performs much better in the CCSM environment, both the underestimation of variability and the systematic bias to higher AMVI values are smaller in the CCSM4 case (cf. Fig. 3e and Fig. B2e). Also, the low-frequency variability is better captured (Fig. B2f). While the full emGPR clearly outperforms the PCR in the MPIESM case, PCR and the full emGPR perform similarly well in the CCSM4 case.

3.2 TCnpp: Noisy pseudoproxies

With the noisy pseudoproxies, the best reconstruction is still achieved by the full emGPR (The superior performance of the PCR in the CCSM4 case can be explained by a greater spatial coherence of the underlying CCSM4 temperature field. The leading EOF explains 41% of the total variance in the CCSM4 case and only 27% in the MPIESM case (not shown). The difference in spatial coherence is also reflected in the overall smaller embedding distances in the CCSM4 case (compare Fig. 4a,e1 and B1). The mean of the 30 noisy reconstructions is remarkably similar to fact that the full and sparse emGPR perform about equally well for MPIESM and CCSM4, indicates that the emGPR is more robust to different degrees of spatial coherence in the underlying field. This can be considered an additional strength of the emGPR.

480 3.2 TCnpp: Noisy pseudoproxies

We calculate the AMVI based on perfect pseudoproxies. The characteristics of the ensemble mean likely gives a too positive evaluation of the reconstruction skill because some of the noise effects will cancel in the averaging process. But also the for each of the 30 noisy reconstructions separately and provide the mean and spread of the ensemble statistics. The distribution of the three skill metrics for each reconstruction method can be found in Appendix C. For the full emGP, the individual ensemble members are still in reasonably good agreement with the target AMVI (see thin lines in Fig. 4a and Fig. C1a for the distribution of skill metrics). The mean correlation of the smoothed ensemble mean reconstructed AMVI with the target AMVI is 0.95 (ensemble range: 0.84 to 0.96) 0.89 ± 0.06 . The mean bias is with 21 ± 0.15 % of the target standard deviation identical, very similar to the bias from the TCnpp case (ensemble range: -37 to -5%), and as before it. As with the TCnpp testcase, the bias mostly stems from the years 1630 to 1680, where the mismatch between the reconstructions and target is largest. The variability is still captured remarkably well. The mean standard deviation ratio for the ensemble mean of 0.95 indicates a slight underestimation of the variability by 5% (ensemble range: 0.86 to 1.16). The underestimation is 1.01 ± 0.17 , indicating that most ensemble reconstructions contain a realistic amount of variability. The main loss of variability occurs mainly at frequencies higher than decadal (Fig. 4b). The lower-frequency variability range, which is of main interest for studying the AMV, is well reconstructed; the reconstructed spectra lie well within the uncertainty range of the target spectrum.

495 The sparse emGPR also performs well with noisy pseudoproxies (Fig. 4c,d and Fig. C1b). The ensemble mean even has a higher reconstruction skill as the AMVI reconstructed from overall reconstruction skill is even higher with noisy than with perfect pseudoproxies. This improved performance is also reflected in the estimated timescale of auto-correlation. The estimate for $l_{f,t}$ is now much closer to the estimate from the full emGP (Fig. 5a). We will come back to this improved performance in Sect. 4. The ensemble mean correlation of the smoothed ensemble mean AMVI with the target AMVI is 0.92

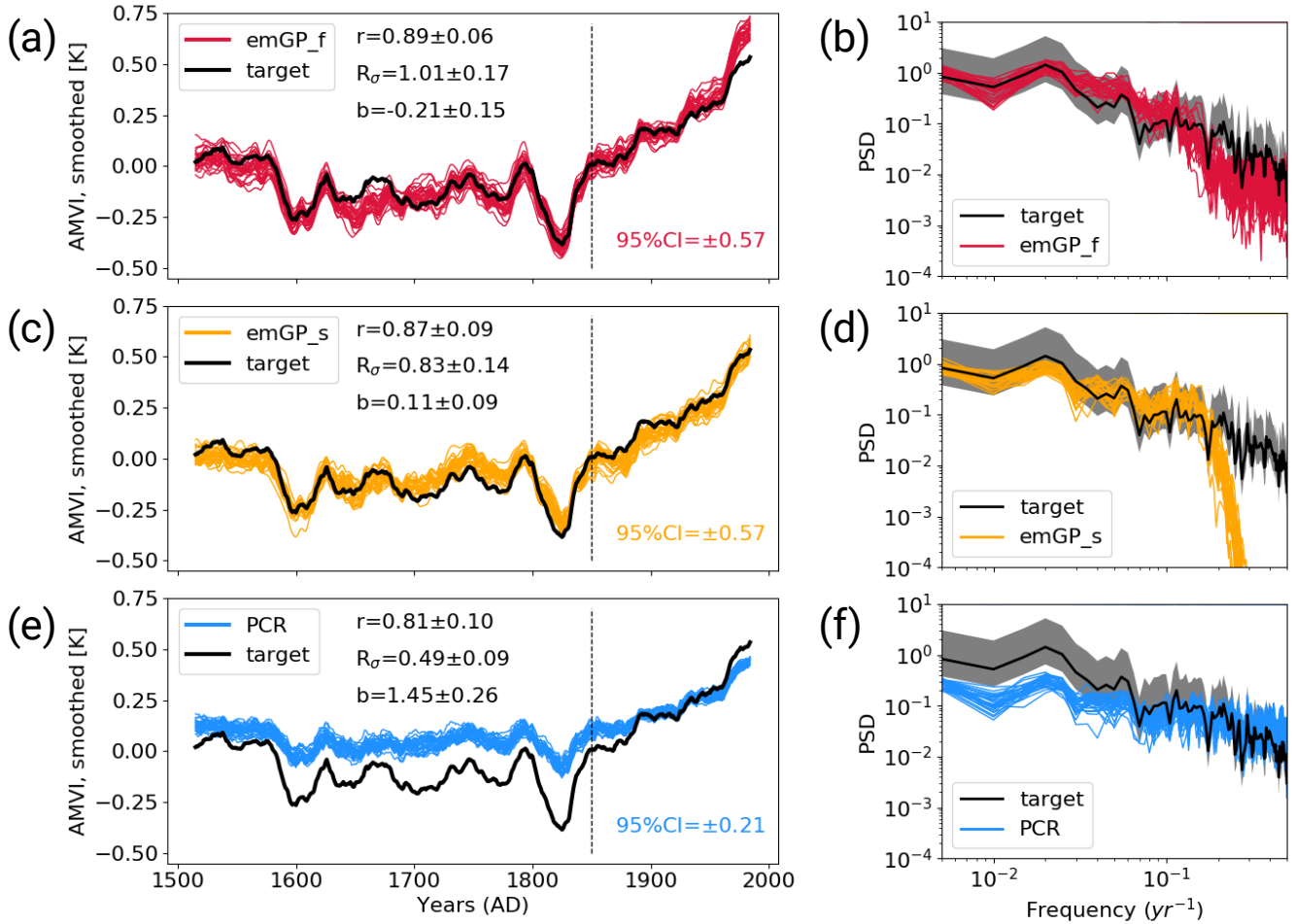


Figure 4. Reconstructions with noisy MPIESM-pseudoproxies based on **(a,b)** the full emGPR, **(c,d)** the sparse emGPR and **(e,f)** PCR. Left-hand panels show the smoothed reconstructed and target timeseries. The dashed line marks the separation between training and testing periods. Thin coloured lines show the individual ensemble members. The 95% CI in the bold line lower right of all three panels indicates the CI averaged over time and all ensemble mean members. The metrics r , R_σ and b denote correlation, ratio of standard deviations and the bias relative to the target standard deviation, respectively. Subscripts sm and yr denote smoothed and unsmoothed data, respectively. The metrics are calculated for the each smoothed ensemble mean during member over the reconstruction period (1500 to 1850), and the mean and spread ($\pm 2\sigma$) are reported here. Right-hand panels show Welch powerspectra power spectra of the target and reconstructed AMVI. Thin coloured lines indicate the spectra of the individual ensemble members, the bold line indicates the spectrum of the ensemble mean. Shading Grey shading indicates the 95% confidence interval of the ensemble mean target spectrum as obtained from the χ^2 -distribution. The power spectral density (PSD) is given in $\text{K}^2 \text{yr}$.

500 (ensemble range: 0.74 to 0.94, Fig. C1b) 0.87 ± 0.09 . Also the mean bias is very small with $11 \pm 0.09\%$ of the target standard deviation (ensemble range: 5 to 18%), only a third of the bias from the TCppp case. The mean standard deviation ratio is 0.78 (ensemble range: 0.70 to 0.98) 0.83 ± 0.14 , corresponding to an underestimation of the variability by $2217 \pm 14\%$. This underestimation is due to a complete loss of power at frequencies higher than decadal (Fig. 4d). But as with the full emGPR, the frequency range of interest for the AMV is well reconstructed.

505 The PCR still achieves high correlations, but suffers a strong underestimation of variability and an increased systematic bias towards the mean of the AMVI over the training period (Fig. 4e,f and Fig. C1c). These deficiencies of the PCR reconstructions with noisy data have been well documented already (e.g., von Storch et al., 2009). The ensemble mean correlation with the smoothed target AMVI is 0.87 (ensemble range: 0.71 to 0.88, Fig. C1c) 0.81 ± 0.10 . The mean bias of $145 \pm 26\%$ exceeds one standard deviation of the target AMVI (ensemble range: 115 to 172%). The mean standard deviation ratio is 0.46 (ensemble 510 range: 0.41 to 0.59) 0.49 ± 0.09 , corresponding to an underestimation of variability by $5451 \pm 9\%$. The loss of variability occurs mainly in the range of frequencies *lower* than decadal, i.e., the frequencies of interest for the AMVI are *underestimated*, severely underestimated (Fig. 4f).

515 The use of noisy pseudoproxies has approximately doubled the width of the 95% confidence intervals for all three methods. The mean uncertainty range over all emGP ensemble members is ± 0.57 , which is again too conservative but reasonable given the amount of non-climatic noise in the pseudoproxies. The mean PCR uncertainty range is ± 0.21 , which is likely too confident in combination with the large reconstruction bias.

Again, the reconstruction results with the noisy CCSM4-based pseudoproxies are broadly consistent with the MPIESM-based reconstructions (Fig. B3 and Fig.). Still, some notable differences occur. The full emGPR has a larger negative mean bias of $7475 \pm 0.17\%$ of the target standard deviation and slightly overestimates the variability on multi-decadal timescales 520 timescales longer than 80 years (Fig. B3a,b). The best reconstruction skill in the noisy CCSM4 case is achieved by the sparse emGPR, with high correlations, a small mean bias and a good estimation of the variability in the decadal to multi-decadal frequency range (Fig. B3c,d). A possible explanation for the higher skill of the sparse emGPR can again be found in the hyperparameters. In the sparse case, the uncertainty from the noisy pseudoproxies was correctly assigned to the noise variance σ_n^2 (Fig. B4c). In the full case, the large proxy noise was instead interpreted as signal variance ($\sigma_{f,r}$, Fig. B4b). We will 525 return to this point in Sect. 4. With noisy pseudoproxies, the PCR shows the same deficiencies as in the MPIESM case: a strong systematic bias towards the mean of the AMVI during the training period and a strong underestimation of variability on timescales longer than decadal AMV-relevant timescales (Fig. B3e,f).

3.3 TCp2k: Realistic PAGES2k proxy availability

Until now, we have assumed that the proxy availability is constant in time. In the following, we assess the reconstruction skill 530 of the two emGPR methods with realistic – i.e., varying – data availability and over the full 2000 years. We do this in three steps: First, we test how the emGPR performs over the full 2000 years with perfect pseudoproxies and constant data availability (i.e., the same as TCppp but over 2000 years). Second, we reconstruct the AMVI with perfect pseudoproxies and realistically varying data availability. To achieve realistic data availability, we clip the annually resolved pseudoproxy records at the start

and end years of the corresponding real-world proxy records from the PAGES2k data-base. And third, we test the emGPR with
535 noisy pseudoproxies and varying data availability. The third step, even though still idealised, is closest to representing realistic
conditions for proxy-based reconstructions.

Because the full and sparse emGPR differ in the amount of computing memory, we use two different approaches to reconstruct the full 2000 years. In our current computing environment and with the selected MPIESM-based proxy network of 23 locations, the full emGPR cannot handle much more than 500 years at a time. We therefore, therefore, train the full emGPR on
540 the most recent 500 years and use the estimated hyperparameters to reconstruct the AMVI piece-wise in the remaining three blocks of 500 years. For the first step, we actually take the hyperparameters from TCppp (red stars in Fig. 5). For the second step, we estimate the hyperparameters again, to see how much they differ when the data availability changes (red diamonds in Fig. 5). For the full emGPR, they turn out to be very similar, therefore, we use the hyperparameters from TCnpp in the third step in order to save computing time (red dots in Fig. 5). The sparse emGPR can be trained and evaluated over the whole
545 2000 years at once with reasonable computational effort. Therefore, we retrain the hyperparameters in each of the three steps – (yellow diamonds in Fig. 5).

3.3.1 Full emGPR

The first step with the full emGPR shows that our approach of piece-wise reconstruction works well. The reconstructed AMVI closely follows the target AMVI also in the years 0 to 1500 (Fig. 6a). This confirms that the hyperparameters estimated from
550 the first 500 years are also representative for of the remaining periods (at least in this MPIESM-based setting). The correlation of the smoothed reconstructed AMVI and the target AMVI is with 0.87, a bit lower as in the TCppp case. The mean bias of 8% of the target standard deviation is smaller than in the TCppp case. The variability is well reconstructed, as indicated by both the standard deviation ratio of 1.03 and and the power spectrum (Fig- 8a).

With variable data availability in the second step, the full emGPR still achieves a similarly high reconstruction skill (Fig. 6b).
555 The correlation of the smoothed reconstructed AMVI and the target AMVI is 0.88 and the mean bias is negligible. Interestingly, the reduced data availability leads to an overestimation of variability in some periods (e.g., in the years 900 to 1100). This is also indicated by the standard deviation ratio of 1.19. This could be attributed to non-optimal hyperparamters for the reduced proxy availability in this period (see Sect. 4). The power spectrum also shows slightly higher power in the multi-decadal frequency range (Fig- 8b). On the other hand, there is a strong loss of power in the high frequency high-frequency range (>
560 1/10 yr^{-1}).

The third step confirms that the full emGPR can achieve high reconstruction skill also under realistic conditions (Fig. 6c and Fig. C2a). The mean correlation of the smoothed ensemble mean AMVI reconstruction with the target AMVI is 0.80 (ensemble range: 0.59 to 0.74) 0.67 \pm 0.07 and the mean bias amounts to 12 \pm 5% of the target standard deviation(ensemble range: 6 to 15%). Many periods of extreme high and low AMVI are well captured (e.g., around year 300 and 1150), but some
565 of these extreme periods are also underestimated (e.g., around year 550). The mean standard deviation ratio of the mean is 0.88(ensemble range: 0.90 to 1.22) is 1.06 \pm 0.15, indicating an underestimation of variability by 22%. The loss of variability mainly occurs again in the high-frequency range, and to some extent also in the very low-frequency range overall realistic level

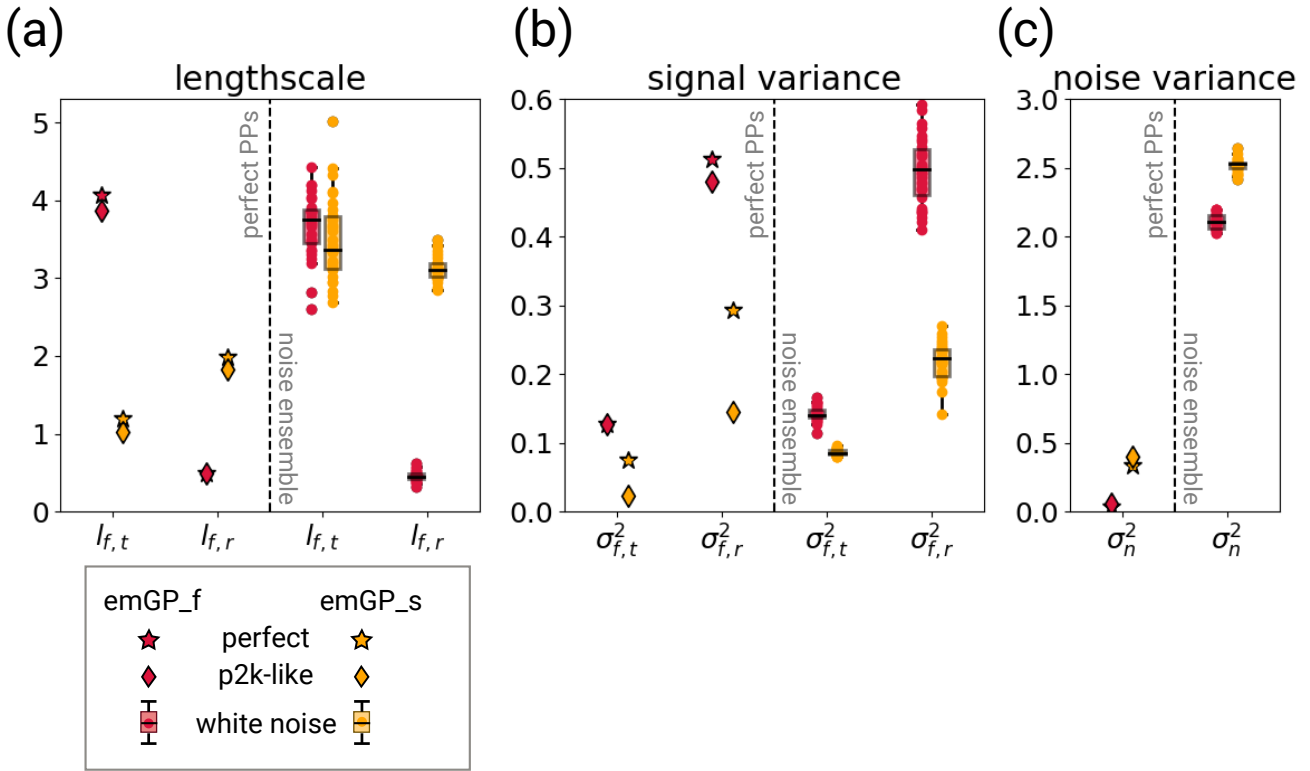


Figure 5. The hyperparameters of the two GPR versions for different training periods with perfect MPIESM-pseudoproxies (left halves of the panels) and the different white noise ensemble members (right halves of the panels). The hyperparameters are (a) the typical lengthscales $l_{f,t}$ and $l_{f,r}$, (b) the signal variance $\sigma_{f,t}^2$ and $\sigma_{f,r}^2$, and (c) the noise variance σ_n^2 . The subscript t indicates that the kernel operates only on the time dimension; the subscript r indicates that the kernel operates on all dimensions, including time (see Eq. 6 and 7). The lengthscales are unitless, corresponding to the unitless distance of the embedding space. The lengthscale $l_{f,t}$ can be transformed into years through division by 1.44. The signal and noise variance are given in K^2 .

of variability. Especially the variability in the decadal to multi-decadal range is still well captured (Fig- 8c). The variability in the decadal to multi-decadal range is still well captured only loss of variability occurs again in the high-frequency range on timescales shorter than decadal.

570

3.3.2 Sparse emGPR

In the first step, the sparse emGPR shows a slightly reduced reconstruction skill as compared with the TCppp case. The mean bias is very small, but the correlation is smaller and the underestimation of variability is stronger (Fig. 7a). The variability is underestimated both on interannual and multi-decadal to centennial timescales (Fig. 8,d).

575

With variable data coverage in the second step, the reconstruction skill of the sparse emGPR remains similar, only the underestimation of variability on multidecadal to centennial timescales increases (Fig. 7b and 8e).

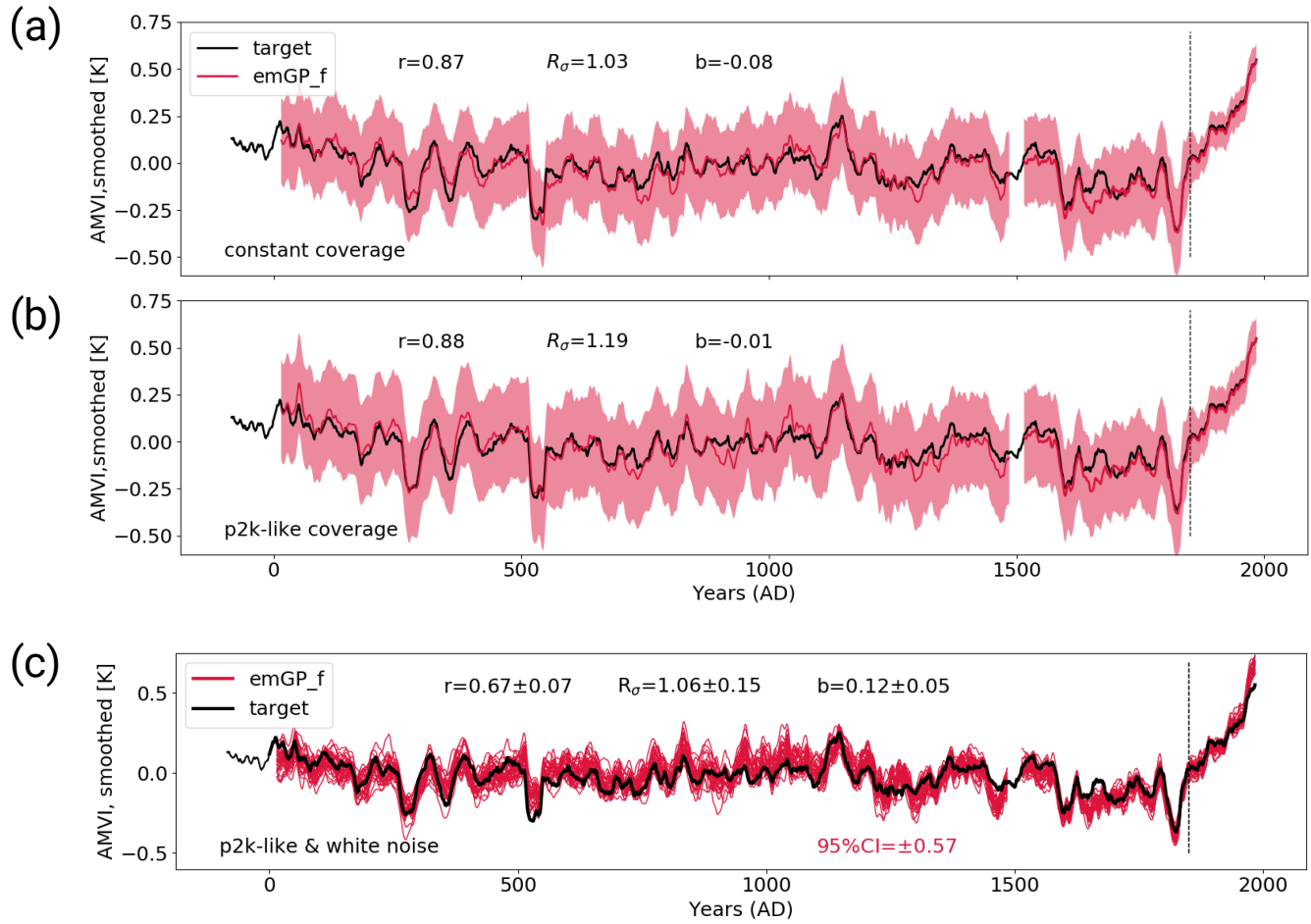


Figure 6. The MPIESM-TCp2k reconstructions with the full emGPR. **(a)** first step with perfect pseudoproxies and constant proxy availability. **(b)** second step with perfect pseudoproxies and realistic proxy availability according to the PAGES2k database. **(c)** third step with white-noise added to the proxies and realistic proxy availability.

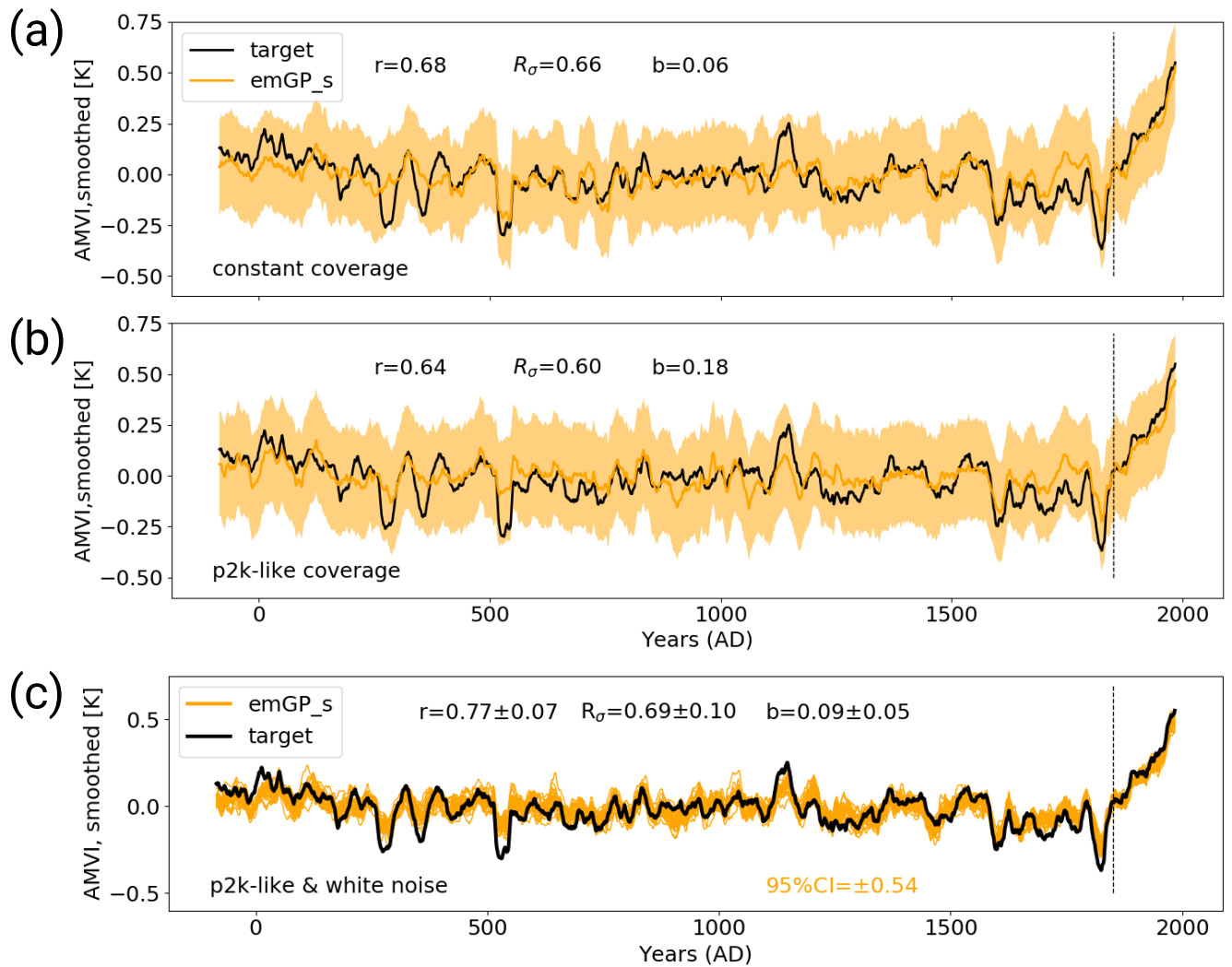


Figure 7. The MPIESM-TCp2k reconstructions with the sparse emGPR. **(a)** first step with perfect pseudoproxies and constant proxy availability. **(b)** second step with perfect pseudoproxies and realistic proxy availability according to the PAGES2k database. **(c)** third step with white-noise added to the proxies and realistic proxy availability.

In the third step, the mean correlation of the smoothed reconstructed ensemble mean AMVI AMVI reconstructions with the target AMVI increases to 0.88 (ensemble range: 0.70 to 0.83) 0.77 ± 0.07 , confirming again that the sparse emGPR seems to capture some details of the AMVI better in the presence of noise (Fig. 7c and Fig. C2b), and the greater flexibility that comes with a high estimate of noise variance in the GP hyperparameters (Fig. 5c). Still, the The underestimation of variability remains large, both on interannual and multi-decadal to centennial timescales (Fig. 8f). The underestimation of variability on multi-decadal timescales is comparable to Even though the sparse emGPR obtains the worst reconstruction skill in this test case, the overall skill is still higher than that of the PCR with full data availability in the TCnpp case.

4 Discussion

We have tested two versions of GPR in a newly developed input space (embedding space) for climate-index reconstructions in pseudoproxy experiments with increasingly realistic conditions. As a benchmark, we used a PCR-based reconstruction. Under perfect conditions (TCppp), all three methods – full and sparse emGPR and PCR – achieve high reconstruction skill. The full emGPR outperforms the sparse emGPR and performs at least as well as the PCR. With noise-contaminated pseudoproxies (TCnpp), the full emGPR has the highest reconstruction skill with a realistic estimate of variability on AMV-relevant timescales – (i.e., decadal to multi-decadal). The sparse emGPR achieves the second best second-best reconstruction skill with a realistic mean but increased variance loss. The PCR-based reconstruction is systematically biased to the AMVI values of the training period and suffers a strong loss of variance on AMV-relevant timescales. With realistic proxy availability and noise-contaminated noise-contaminated pseudoproxies (3rd step of TCp2k), the full emGPR is still able to achieve a high reconstruction skill with a realistic (ensemble) mean and variability on AMV-relevant timescales. Below, we re-assess the overall performance of the methods, give possible explanations for differences in reconstruction skill and discuss the wider applicability of the emGP.

4.1 Non-climatic noise

Our results indicate that the emGPR (both full and sparse) is able to perform well in the presence of non-climatic noise. This property can most likely be explained by the hyperparameter of the noise variance σ_n^2 (Fig. 5c). The noise variance describes the uncertainty in the regression targets. This concept can only be meaningfully applied here because we perform the GPR in the embedding space, where both the proxy timeseries and the AMVI are the regression targets. The noise variance can therefore, therefore, capture the non-climatic signal of the pseudoproxies and give the emGPR the necessary flexibility to filter the non-climatic part of the signal. Comparing the noise variance between the TCppp and TCnpp cases illustrates this quite well. In the TCppp case, the estimated noise variance (or likelihood) σ_n^2 lies between 0.1 and 0.4 K². In the TCnpp case, the estimated σ_n^2 lies between 2 and 2.7 K². This does reflect the actual mean magnitude of the noise which we added to the pseudoproxies. The mean variance of the noise of all 23 records is approximately 2.1 K² (for the individual records, the variance of the added noise ranges from 0.3 K² to 4.9 K²). Thus, the GPR training procedure seems to be able to learn a realistic magnitude of the added noise.

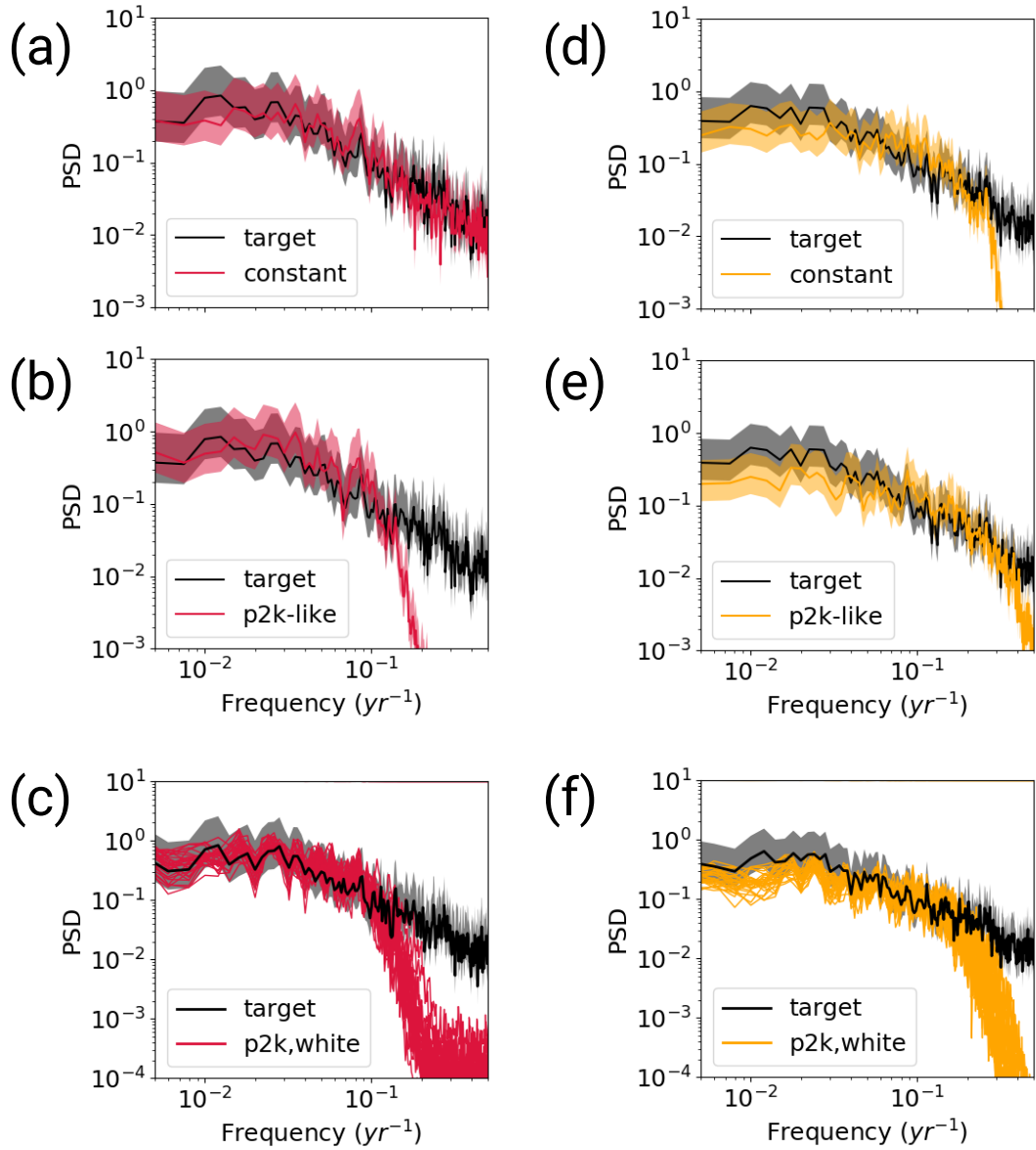


Figure 8. Welch power spectra of the MPIESM-TCp2k reconstructions for the full (red) and sparse (yellow) emGPR. **(a,d)** first step with perfect pseudoproxies and constant proxy availability. **(b,e)** second step with perfect pseudoproxies and realistic proxy availability according to the PAGES2k database. **(c,f)** third step with white-noise added to the proxies and realistic proxy availability. [grey shading indicates the 95% confidence interval of the target spectrum](#). The power spectral density (PSD) is given in $\text{K}^2 \text{ yr}$.

Interestingly, the increased flexibility of the GP through the higher σ_n^2 not only yields robust reconstructions in the presence of uncertain pseudoproxies, it also seems to improve the performance of the sparse emGPR—~~at least for the cases with ideal proxy availability (TCnpp)~~. It is possible that the presence of noise makes the sparse emGP less sensitive to overfitting. To test this, we have repeated TC_{ppp} and TC_{npp} for the sparse emGP with a network consisting of only half the number of pseudoproxies (randomly selected from the original networks). We would expect the difference in skill to decrease with the smaller networks, if overfitting was indeed the reason. The difference between the reconstruction with perfect and noisy data is indeed reduced with respect to the full networks (Fig. D1). The TC_{ppp} reconstruction has a comparable reconstruction skill to single TC_{npp} reconstruction members with both MPIESM and CCSM4-based pseudoproxies. We, therefore, conclude that the improved performance of the sparse emGP with noisy data can at least partly be attributed to a greater robustness against overfitting in the presence of noise.

Here, we have only tested white-noise pseudoproxies, i.e. we assume that the noise in the pseudoproxy records is not correlated in time. The typical noise model for σ_n^2 , which we apply here, also works with the assumption of uncorrelated Gaussian white noise. For real proxies this may not always be the case. There are ways of adapting the noise model to include, e.g., correlated noise (see Rasmussen and Williams, 2006). The embedding space would be a good starting point for this, as we explicitly take the time dimension into account. The noise model would introduce additional hyperparameters and make the calibration more complex. If we simply used our current set-up with correlated noise, the model might interpret some of the noise correlation incorrectly as actual data-correlation. This could be the subject of a follow-up study.

625 4.2 Hyperparameter estimation and overfitting

The full emGPR achieves generally higher reconstruction skill than the sparse emGPR (one exception is the TC_{npp} case with ~~ECM4-based~~_{CCSM4-based} pseudoproxies). This could be expected, since the sparse emGPR approximates the covariance matrix based on only a tenth of the available training data, i.e. the subset of selected inducing points. Possibly, the hyperparameters are more accurately learned from the full dataset. Another possibility is that the location of the inducing points in 630 non-optimal. We have initialised the inducing points as every tenth step in time and then optimised the location during training. We have not tested other setups of the inducing points. It is possible that a higher number or differently selected inducing points would result in a higher reconstruction skill.

The optimisation of the hyperparameters is an additional source of uncertainty. The learned set of hyperparameters may not always be the optimal set. We did not make any sensitivity tests regarding e.g. initialisation of the hyperparameters. But the fact 635 that the training of the full emGPR resulted in similar hyperparameters for all three MPIESM-based test cases (TC_{ppp}, TC_{npp} and TC_{p2k}) gives us confidence that the estimated hyperparameters for the full emGPR are accurate. The hyperparameters that ~~can be interpreted physically~~ have a straightforward physical interpretation, i.e. the ~~typical lengthscale of the kernel over the time dimension~~ typical lengthscale $l_{f,t}$ and variance $\sigma_{f,t}^2$ of the first kernel and the noise variance σ_n^2 , also appear reasonable in their magnitudes in most cases ~~—(red stars in Fig. 5)~~. The timescale of the full emGP is on the order of 2.7 years, which is 640 a reasonable timescale of auto-correlation. As discussed above, σ_n^2 captures the magnitude of the mean added noise variance across all records. The signal variance $\sigma_{f,t}^2 = 0.12$ indicates a temporal temperature variability of approximately 0.35 K. For all

selected pseudoproxies, the temporal variability ranges from 0.28 to 1.15 K. The estimated $\sigma_{f,t}$ is thus on the lower end of plausible values. The timescale $l_{f,r}$ and variance $\sigma_{f,r}^2$ of the second kernel are less straightforward to interpret, as they operate across space and time. However, $\sigma_{f,r}^2$ should somehow reflect the mean temperature variability across all records and time. The estimate of $\sigma_{f,r}^2=0.51$ indicates a variability of 0.71. This is a fairly close estimate of the actual 0.82 K of the underlying data.

Based on the comparison of the hyperparameters across all experiments, we identify two possible cases of non-optimal hyperparameters: (1) First, the TC_{ppp} case with the sparse emGPR, based on both MPIESM and CCSM4 pseudoproxies. Here, the estimated typical timescale $l_{f,t}$ is much shorter than that estimated from the full emGPR (left halves of Fig. 5a and Fig. B4a). (2) And second, the TC_{npp} case with the full emGPR and CCSM4-based pseudoproxies. In this case, the noise variance was not ~~identified correctly~~ correctly estimated. Instead, the noise variance was attributed to the signal variance $\sigma_{f,r}^2$. The values of σ_n^2 and $\sigma_{f,r}^2$ appear switched compared to the other TC_{npp} experiments (compare right halves of Fig. B4b and c, and Fig. 5b and c). Repeating the CCSM4-based TC_{npp} experiment with switched σ_n^2 and $\sigma_{f,r}^2$ slightly increases the reconstruction skill, but the skill remains lower than for the TC_{npp} with the sparse emGPR (not shown). This illustrates how difficult it is to find an optimal set of hyperparameters.

The skill of As with all reconstruction methods, it is possible that the (hyper)parameters learned during training are not completely representative for the reconstruction period. To test for the non-stationarity of hyperparameters in case of changing proxy availability, we have repeated the TC_{p2k} experiment with the full emGP for the years 1000-1500 (Fig. D2). The new hyperparameters indicate a smaller signal variance and shorter auto-correlation timescale (red and grey diamonds in Fig. D3). This improves the reconstruction skill with respect to the original TC_{p2k} experiment. However, non-stationary hyperparameters are difficult to account for with real-world data. By training the emGP with the maximum of available proxy data, we try to get the best mean estimate, but cannot fully avoid the effect of non-stationarity.

4.3 Embedding distance

As well as the hyperparameters, also the embedding distances are not constant in time (Fig. D4). Changing cross-correlations may lead to under- or overestimation of individual records during certain periods. Again, this is something which is difficult to account for with real world data, and by calculating the embedding distance over the entire periods of proxy availability we try to find the best mean distance estimate.

Another source of uncertainty is the choice of the distance metric on which the creation of the embedding space is based. We have tested equidistant coordinates, cross-correlation and cross-correlation with standard deviation ratio and selected the latter metric. But of course, other ways of constructing the embedding space could be possible. The optimal embedding space may differ for each proxy network and proxy properties. This is definitely worthy of further investigation.

4.4 Climate model dependence

The skill of all three methods, including the benchmark PCR, depends to some degree also on the climate model from which the pseudoproxies are derived. This is a known issue (Smerdon et al., 2011). The full emGPR performs better in the MPIESM-based experiments, the PCR performs better in the CCSM4-based experiments and the sparse emGPR performs about equally well in

675 both model worlds. Source of the different skill could be the differences in the network size and location of the pseudoproxies and differences in the cross-correlation structure. It is ~~of course~~, of course, difficult to say, whether a reconstruction with real proxies will behave more like the MPIESM-based experiments or more like the CCSM4-based experiments. But regardless of the differences in skill, the fact that the emGPR has higher reconstruction skill in the more realistic TCnpp case and suffers from a much smaller variability loss than the PCR in both model worlds, ~~makes~~ gives us confidence that emGPR will also
680 improve the reconstructed variability in a real reconstruction.

~~A last source of uncertainty is the choice of the distance metric on which the creation of the embedding space is based. We have tested equidistant coordinates, cross-correlation and cross-correlation with standard deviation ratio and selected the latter metric. But of course other ways of constructing the embedding space could be possible. The optimal embedding space may differ for each proxy network and proxy properties. This is definitely worthy of further investigation.~~

685 The

4.5 Using real proxies and wider applications

690 ~~The~~ pseudoproxy experiments give a good first impression of how the reconstructions may behave with real proxies. Nonetheless, even though the third step of TCp2k (noise contamination and variable proxy coverage) is already quite realistic, it is still idealised. E.g. in the pseudoproxy setup, we calculate the distance matrix \mathbf{D} based on the whole length of the simulation. With real proxies, each proxy record has a different length and covers a different period. In this case, the distance matrix could be calculated based either on a common time period where all records are available (this could be a very short period), or it could be the period of overlap for each individual pair of records. ~~In the~~

695 ~~In principle, the framework presented here can be applied to any climate index that exhibits significant correlations with local proxy sites. It is thus not limited to the AMVI application presented here. With real proxies, that do not all come in units of $^{\circ}\text{C}$ (e.g., lake sediments, tree ring width, isotope ratios), it might make more sense to standardise all records to unit variance. In this case, the embedding distance would no longer need to include the SR-scaling. A simple dependence on the CC might be sufficient. This remains to be tested.~~

700 ~~In order to use this framework for indexes that operate on longer timescales, it might become necessary to include records with lower temporal resolution. This would require subsampling of all records to the lowest common resolution, which is common practice in long-term reconstructions. It might also be possible to train one emGP model for the high-resolution records and one for the low resolution-records. The caveat here is that the observational period is often too short to include enough training data for the low-resolution records. But this is true for all reconstruction methods and not unique to the emGP framework here.~~

705 ~~In the TCnpp cases, we created 30 different white noise realisations to estimate the noise-related uncertainty. With real proxies, we ~~of course~~, of course, only have one realisation of the data and cannot run noise ensembles. But one could think of other ways of generating ensembles, e.g. with slightly different hyperparameters or ~~or~~, slightly different ways of constructing the distance matrix or inclusion of different noise models for σ_n^2 . This would instead give insight into the other more methodological sources of uncertainty.~~

5 Conclusions

710 We have developed and tested a new method for proxy-based climate-index reconstruction. Our aim was to reduce the under-
estimation of variability on AMV-relevant timescales (decadal to multi-decadal), which is a common drawback of established
reconstruction techniques such as PCR. To this end, we applied Gaussian Process regression and developed a modified in-
put space, which we denoted embedding space. We tested two versions of GPR, a full version and a stochastic variational,
i.e. sparse, version. The full version is generally more accurate but comes at high computational costs and can only handle a
715 limited amount of data. As a benchmark comparison, we also computed AMVI reconstructions with PCR.

Under ideal conditions (TCppp: pseudoproxies contain only the climate signal, all records available over the entire recon-
struction period), the full embedded GPR performs at least as well as the PCR; in the pseudoproxy experiments based on
MPIESM the embedded GPR achieves an even higher reconstruction skill and suffers almost no variance loss. Under more
720 realistic conditions (TCnpp: pseudoproxies contaminated with non-climatic white noise, all records available over the entire
reconstruction period), the reconstructions skill of the PCR strongly decreases, and both the full and the sparse embedded GPR
clearly outperform the PCR. The GP-based reconstructions have an overall small mean bias and reconstruct the variability on
AMV-relevant timescales much more accurately. Under even more realistic conditions (TCp2k: pseudoproxies contaminated
725 with non-climatic white noise, records have different length and cover different periods), the sparse embedded GPR still has an
overall small mean bias but suffers a strong variance loss, while the full embedded GPR is still capable of reconstructing the
variability on the timescales of interest accurately.

Of course, it remains to be seen how the embedded GPR performs with real proxies. As a next step, we will perform a real
AMVI reconstruction based on the PAGES2k proxy network. Based on the results presented in this study, we are confident that
climate-index reconstructions can be significantly improved with embedded GPR. A more accurate reconstruction of the mean
730 state and the magnitude of variability will help *in advancing* our understanding of AMV dynamics, e.g., especially
during periods of extreme cooling following volcanic eruptions.

Code and data availability. The extracted pseudoproxy data and the simulated AMVI from the MPIESM and CCSM4 simulations as well as
the python scripts for the preparation of the pseudoproxy network, the preparation of the embedding space and the GP regression are provided
in the supplement of the paper. The used Python packages Scikit-learn (v.0.19.1), TensorFlow (v.1.12.0) and GPflow (v.1.3.0) are publicly
735 available. The PAGES2k database can be downloaded here: <https://doi.org/10.6084/m9.figshare.c.3285353>. The CCSM4 past1000 and histor-
ical simulations can be obtained from the World Data Center for Climate (doi:10.1594/WDCC/CMIP5.NRS4pk and doi:10.1594/WDCC/CMIP5.NRS4hi,
respectively).

Author contributions. MK and EZ conceptualised the study. UvT developed the concept of the embedding space. MK implemented the code,
performed the pseudo-reconstructions, analysed the results and wrote the first draft of the manuscript. All authors discussed the results and
contributed to writing the manuscript.

Acknowledgements. This study has been performed in the context of RedMod (redmod-project.de), a project funded by the Helmholtz Inkubator initiative. The emGPR reconstruction code was run on the gpu nodes of the supercomputer *Mistral* at the German Climate Computing Centre (DKRZ). The MPIESM simulation was run by Sebastian Wagner (Helmholtz-Zentrum Hereon). The analysis was enabled and facilitated by the open-source Python packages Scikit-learn (Pedregosa et al., 2011), TensorFlow (Abadi et al., 2015) and GPflow (Hensman et al., 745 2013). Figures were generated with Matplotlib (Hunter, 2007).

References

Abadi, M., Agarwal, A., Barham, P., Brevdo, E., Chen, Z., Citro, C., Corrado, G. S., Davis, A., Dean, J., Devin, M., Ghemawat, S., Goodfellow, I., Harp, A., Irving, G., Isard, M., Jia, Y., Jozefowicz, R., Kaiser, L., Kudlur, M., Levenberg, J., Mané, D., Monga, R., Moore, S., Murray, D., Olah, C., Schuster, M., Shlens, J., Steiner, B., Sutskever, I., Talwar, K., Tucker, P., Vanhoucke, V., Vasudevan, V., Viégas, F., Vinyals, O., Warden, P., Wattenberg, M., Wicke, M., Yu, Y., and Zheng, X.: TensorFlow: Large-Scale Machine Learning on Heterogeneous Systems, <https://www.tensorflow.org/>, software available from tensorflow.org, 2015.

750 Barboza, L., Li, B., Tingley, M. P., and Viens, F. G.: Reconstructing past temperatures from natural proxies and estimated climate forcings using short- and long-memory models, *The Annals of Applied Statistics*, pp. 1966–2001, 2014.

Büntgen, U., Allen, K., Anchukaitis, K. J., Arseneault, D., Boucher, É., Bräuning, A., Chatterjee, S., Cherubini, P., Churakova, O. V., Corona, 755 C., Gennaretti, F., Grießinger, J., Guillet, S., Guiot, J., Gunnarson, B., Helama, S., Hochreuther, P., Hughes, M. K., Huybers, P., Kirdyanov, A. V., Krusic, P. J., Ludescher, J., Meier, W. J.-H., Myglan, V. S., Nicolussi, K., Oppenheimer, C., Reinig, F., Salzer, M. W., Seftigen, K., Stine, A. R., Stoffel, M., St. George, S., Tejedor, E., Trevino, A., Trouet, V., Wang, J., Wilson, R., Yang, B., Xu, G., and Esper, J.: The influence of decision-making in tree ring-based climate reconstructions, *Nature communications*, 12, 1–10, 2021.

Christiansen, B., Schmitt, T., and Thejll, P.: A surrogate ensemble study of climate reconstruction methods: Stochasticity and robustness, 760 *Journal of Climate*, 22, 951–976, <https://doi.org/10.1175/2008JCLI2301.1>, 2009.

Clement, A., Bellomo, K., Murphy, L. N., Cane, M. A., Mauritsen, T., Rädel, G., and Stevens, B.: The Atlantic Multidecadal Oscillation without a role for ocean circulation, *Science*, 350, 320–324, <https://doi.org/10.1126/science.aab3980>, 2015.

Duvenaud, D., Lloyd, J., Grosse, R., Tenenbaum, J., and Zoubin, G.: Structure discovery in nonparametric regression through compositional kernel search, in: International Conference on Machine Learning, edited by Dasgupta, S. and McAllester, D., vol. 28 of *Proceedings of Machine Learning Research*, pp. 1166–1174, PMLR, Atlanta, Georgia, USA, <https://proceedings.mlr.press/v28/duvenaud13.html>, 2013.

765 Esper, J., Frank, D. C., Wilson, R. J., and Briffa, K. R.: Effect of scaling and regression on reconstructed temperature amplitude for the past millennium, *Geophysical Research Letters*, 32, <https://doi.org/10.1029/2004GL021236>, 2005.

Garuba, O. A., Lu, J., Singh, H. A., Liu, F., and Rasch, P.: On the relative roles of the atmosphere and ocean in the Atlantic multidecadal variability, *Geophysical Research Letters*, 45, 9186–9196, <https://doi.org/10.1029/2018GL078882>, 2018.

770 Gent, P. R., Danabasoglu, G., Donner, L. J., Holland, M. M., Hunke, E. C., Jayne, S. R., Lawrence, D. M., Neale, R. B., Rasch, P. J., Vertenstein, M., et al.: The community climate system model version 4, *Journal of climate*, 24, 4973–4991, <https://doi.org/10.1175/2011JCLI4083.1>, 2011.

Giorgetta, M. A., Jungclaus, J., Reick, C., Legutke, S., Bader, J., Böttinger, M., Brovkin, V., Crueger, T., Esch, M., Fieg, K., Glushak, K., 775 Gayler, V., Haak, H., Hollweg, H.-D., Ilyina, T., Kinne, S., Kornblueh, L., Matei, D., Mauritsen, T., Mikolajewicz, U., Mueller, W., Notz, D., Pithan, F., Raddatz, T., Rast, S., Redler, R., Roeckner, E., Schmidt, H., Schnur, R., Segschneider, J., Six, K., Stockhause, M., Timmreck, C., Wegner, J., Widmann, H., Wieners, K., Claussen, M., Marotzke, J., and Stevens, B.: Climate and carbon cycle changes from 1850 to 2100 in MPI-ESM simulations for the Coupled Model Intercomparison Project phase 5, *Journal of Advances in Modeling Earth Systems*, 5, 572–597, <https://doi.org/10.1002/jame.20038>, 2013.

Gray, S. T., Graumlich, L. J., Betancourt, J. L., and Pederson, G. T.: A tree-ring based reconstruction of the Atlantic Multidecadal Oscillation since 1567 AD, *Geophysical Research Letters*, 31, <https://doi.org/10.1029/2004GL019932>, 2004.

780 Hanhijärvi, S., Tingley, M. P., and Korhola, A.: Pairwise comparisons to reconstruct mean temperature in the Arctic Atlantic Region over the last 2,000 years, *Climate Dynamics*, 41, 2039–2060, <https://doi.org/10.1007/s00382-013-1701-4>, 2013.

Haustein, K., Otto, F. E., Venema, V., Jacobs, P., Cowtan, K., Hausfather, Z., Way, R. G., White, B., Subramanian, A., and Schurer, A. P.: A limited role for unforced internal variability in twentieth-century warming, *Journal of Climate*, 32, 4893–4917, 785 <https://doi.org/10.1175/JCLI-D-18-0555.1>, 2019.

Hensman, J., Fusi, N., and Lawrence, N. D.: Gaussian processes for Big data, in: *Proceedings of the Twenty-Ninth Conference on Uncertainty in Artificial Intelligence*, pp. 282–290, <https://arxiv.org/abs/1309.6835>, 2013.

Hunter, J. D.: Matplotlib: A 2D graphics environment, *Computing in Science & Engineering*, 9, 90–95, 790 <https://doi.org/10.1109/MCSE.2007.55>, 2007.

Jones, P. D. and Mann, M. E.: Climate over past millennia, *Reviews of Geophysics*, 42, <https://doi.org/10.1029/2003RG000143>, 2004.

Kingma, D. P. and Ba, J.: Adam: A method for stochastic optimization, *arXiv preprint arXiv:1412.6980*, 2014.

Knudsen, M. F., Jacobsen, B. H., Seidenkrantz, M.-S., and Olsen, J.: Evidence for external forcing of the Atlantic Multidecadal Oscillation since termination of the Little Ice Age, *Nature Communications*, 5, 1–8, <https://doi.org/10.1038/ncomms4323>, 2014.

Kopp, R. E., Kemp, A. C., Bittermann, K., Horton, B. P., Donnelly, J. P., Gehrels, W. R., Hay, C. C., Mitrovica, J. X., Morrow, E. D., and Rahmstorf, S.: Temperature-driven global sea-level variability in the Common Era, *Proceedings of the National Academy of Sciences*, 795 113, E1434–E1441, <https://doi.org/10.1073/pnas.1517056113>, 2016.

Landrum, L., Otto-Btiesner, B. L., Wahl, E. R., Conley, A., Lawrence, P. J., Rosenbloom, N., and Teng, H.: Last millennium climate and its variability in CCSM4, *Journal of climate*, 26, 1085–1111, <https://doi.org/10.1175/JCLI-D-11-00326.1>, 2013.

Mann, M. E., Zhang, Z., Hughes, M. K., Bradley, R. S., Miller, S. K., Rutherford, S., and Ni, F.: Proxy-based reconstructions of hemispheric and global surface temperature variations over the past two millennia, *Proceedings of the National Academy of Sciences*, 105, 13 252–800 13 257, <https://doi.org/10.1073/pnas.0805721105>, 2008.

Mann, M. E., Steinman, B. A., Brouillette, D. J., and Miller, S. K.: Multidecadal climate oscillations during the past millennium driven by volcanic forcing, *Science*, 371, 1014–1019, <https://doi.org/10.1126/science.abc5810>, 2021.

Mann, M. E., Steinman, B. A., Brouillette, D. J., Fernandez, A., and Miller, S. K.: On The Estimation of Internal Climate Variability During 805 the Preindustrial Past Millennium, *Geophysical Research Letters*, n/a, e2021GL096596, <https://doi.org/10.1029/2021GL096596>, 2022.

Mansfield, L. A., Nowack, P. J., Kasoar, M., Everitt, R. G., Collins, W. J., and Voulgarakis, A.: Predicting global patterns of long-term climate change from short-term simulations using machine learning, *npj Climate and Atmospheric Science*, 3, 1–9, <https://doi.org/10.1038/s41612-020-00148-5>, 2020.

Matthews, A. G. d. G., Van Der Wilk, M., Nickson, T., Fujii, K., Boukouvalas, A., León-Villagrá, P., Ghahramani, Z., and Hensman, J.: 810 GPflow: A Gaussian Process Library using TensorFlow., *J. Mach. Learn. Res.*, 18, 1–6, <http://jmlr.org/papers/v18/16-537.html>, 2017.

Mead, A.: Review of the Development of Multidimensional Scaling Methods, *Journal of the Royal Statistical Society. Series D (The Statistician)*, 41, 27–39, <https://doi.org/10.2307/2348634>, 1992.

Meehl, J.: CCSM4 coupled run for CMIP5 historical (1850–2005), World Data Center for Climate (WDCC) at DKRZ [dataset], <https://doi.org/10.1594/WDCC/CMIP5.NRS4hi>, 2014.

Mette, M. J., Wanamaker Jr, A. D., Retelle, M. J., Carroll, M. L., Andersson, C., and Ambrose Jr, W. G.: Persistent multidecadal variability 815 since the 15th century in the southern Barents Sea derived from annually resolved shell-based records, *Journal of Geophysical Research: Oceans*, p. e2020JC017074, <https://doi.org/10.1029/2020JC017074>, 2021.

Michel, S., Swingedouw, D., Chavent, M., Ortega, P., Mignot, J., and Khodri, M.: Reconstructing climatic modes of variability from proxy records using ClimIndRec version 1.0, *Geoscientific Model Development*, 13, 841–858, <https://doi.org/10.5194/gmd-13-841-2020>, 2020.

820 Miles, M. W., Divine, D. V., Furevik, T., Jansen, E., Moros, M., and Ogilvie, A. E.: A signal of persistent Atlantic multidecadal variability in Arctic sea ice, *Geophysical Research Letters*, 41, 463–469, <https://doi.org/10.1002/2013GL058084>, 2014.

Otto-Bliesner, B.: CCSM4 coupled simulation for CMIP5 past 1000 years (850–1850) with natural forcings, World Data Center for Climate (WDCC) at DKRZ [dataset], <https://doi.org/10.1594/WDCC/CMIP5.NRS4pk>, 2014.

PAGES2k: A global multiproxy database for temperature reconstructions of the Common Era, *Scientific Data*, 4, 825 <https://doi.org/10.1038/sdata.2017.88>, 2017.

PAGES2k: Consistent multi-decadal variability in global temperature reconstructions and simulations over the Common Era, *Nature Geoscience*, 12, 643, <https://doi.org/10.1038/s41561-019-0400-0>, 2019.

Pedregosa, F., Varoquaux, G., Gramfort, A., Michel, V., Thirion, B., Grisel, O., Blondel, M., Prettenhofer, P., Weiss, R., Dubourg, V., et al.: Scikit-learn: Machine learning in Python, *Journal of machine learning research*, 12, 2825–2830, 2011.

830 Rasmussen, C. E. and Williams, C. K. I.: Gaussian processes for machine learning, vol. 2, MIT press Cambridge, MA, 2006.

Saenger, C., Cohen, A. L., Oppo, D. W., Halley, R. B., and Carilli, J. E.: Surface-temperature trends and variability in the low-latitude North Atlantic since 1552, *Nature Geoscience*, 2, 492–495, <https://doi.org/10.1038/ngeo552>, 2009.

Särkkä, S.: Bayesian filtering and smoothing, 3, Cambridge University Press, 2013.

Singh, H. K., Hakim, G. J., Tardif, R., Emile-Geay, J., and Noone, D. C.: Insights into Atlantic multidecadal variability using the Last 835 Millennium Reanalysis framework, *Climate of the Past*, 14, 157–174, <https://doi.org/10.5194/cp-14-157-2018>, 2018.

Smerdon, J. E.: Climate models as a test bed for climate reconstruction methods: pseudoproxy experiments, *Wiley Interdisciplinary Reviews: Climate Change*, 3, 63–77, <https://doi.org/10.1002/wcc.149>, 2012.

Smerdon, J. E., Kaplan, A., Zorita, E., González-Rouco, J. F., and Evans, M.: Spatial performance of four climate field reconstruction methods targeting the Common Era, *Geophysical research letters*, 38, <https://doi.org/10.1029/2011GL047372>, 2011.

840 Svendsen, L., Hetzinger, S., Keenlyside, N., and Gao, Y.: Marine-based multiproxy reconstruction of Atlantic multidecadal variability, *Geophysical Research Letters*, 41, 1295–1300, <https://doi.org/10.1002/2013GL059076>, 2014.

Von Storch, H., Zorita, E., Jones, J. M., Dimitriev, Y., González-Rouco, F., and Tett, S. F.: Reconstructing past climate from noisy data, *Science*, 306, 679–682, <https://doi.org/10.1126/science.1096109>, 2004.

von Storch, H., Zorita, E., and González-Rouco, F.: Assessment of three temperature reconstruction methods in the virtual reality of a climate 845 simulation, *International Journal of Earth Sciences*, 98, 67–82, <https://doi.org/10.1007/s00531-008-0349-5>, 2009.

Wang, J., Yang, B., Ljungqvist, F. C., Luterbacher, J., Osborn, T. J., Briffa, K. R., and Zorita, E.: Internal and external forcing of multidecadal Atlantic climate variability over the past 1,200 years, *Nature Geoscience*, 10, 512–517, <https://doi.org/10.1038/ngeo2962>, 2017.

Wegmann, M. and Jaume-Santero, F.: Artificial intelligence achieves easy-to-adapt nonlinear global temperature reconstructions using minimal local data, *Communications earth & environment*, 4, 217, <https://doi.org/10.1038/s43247-023-00872-9>, 2023.

850 Yan, X., Zhang, R., and Knutson, T. R.: A multivariate AMV index and associated discrepancies between observed and CMIP5 externally forced AMV, *Geophysical Research Letters*, 46, 4421–4431, <https://doi.org/10.1029/2019GL082787>, 2019.

Zhang, R. and Delworth, T. L.: Impact of Atlantic multidecadal oscillations on India/Sahel rainfall and Atlantic hurricanes, *Geophysical Research Letters*, 33, L17 712, <https://doi.org/10.1029/2006GL026267>, 2006.

Zhang, R., Delworth, T. L., and Held, I. M.: Can the Atlantic Ocean drive the observed multidecadal variability in Northern Hemisphere 855 mean temperature?, *Geophysical Research Letters*, 34, L02 709, <https://doi.org/10.1029/2006GL028683>, 2007.

Zhang, R., Sutton, R., Danabasoglu, G., Kwon, Y.-O., Marsh, R., Yeager, S. G., Amrhein, D. E., and Little, C. M.: A review of the role of the Atlantic meridional overturning circulation in Atlantic multidecadal variability and associated climate impacts, *Reviews of Geophysics*, 57, 316–375, <https://doi.org/10.1029/2019RG000644>, 2019.

Zhang, Z., Wagner, S., Klockmann, M., and Zorita, E.: Evaluation of statistical climate reconstruction methods based on pseudoproxy experiments using linear and machine learning methods, *Climate of the Past Discussions*, 2022, 1–31, <https://doi.org/10.5194/cp-2022-5>, <https://cp.copernicus.org/preprints/cp-2022-5/>, 2022.

Zorita, E., González-Rouco, F., and Legutke, S.: Testing the approach to paleoclimate reconstructions in the context of a 1000-yr control simulation with the ECHO-G coupled climate model, *Journal of Climate*, 16, 1378–1390, [https://doi.org/10.1175/1520-0442\(2003\)16<1378:TTMEAA>2.0.CO;2](https://doi.org/10.1175/1520-0442(2003)16<1378:TTMEAA>2.0.CO;2), 2003.

Given a set of observed data $\mathbf{y} = y_i = f(\mathbf{x}_i)$, the objective is to provide the probability distribution at a yet unobserved data point \mathbf{z} , $f(\mathbf{z})$, conditional on the available observations. This is achieved by the application of the Bayes theorem. Before the application of Bayes theorem, the prior for $f(\mathbf{z})$ is just the assumed probability distribution for the Gaussian process, with mean $\mu_{prior}(\mathbf{z})$ and variance $cov_{prior} = k(\mathbf{z}, \mathbf{z})$. Usually, μ_{prior} is assumed to be zero without loss of generality (e.g. 870 by taking anomalies from the mean). It is also assumed that observations are a realisation of a *noisy* Gaussian process, which are contaminated by uncertainty in observations, i.e. $y_i = f(\mathbf{x}_i) + \epsilon$. The noise ϵ is assumed to be Gaussian with variance σ_n^2 and uncorrelated across the locations \mathbf{x}_i . After the application of Bayes theorem, the mean and variance can be calculated according to the following predictive equations (for a detailed derivation see Rasmussen and Williams, 2006):

$$\mu_{post}(\mathbf{z}) = k(\mathbf{z}, \mathbf{x})^T [k(\mathbf{x}, \mathbf{x}) + \sigma_n^2 \mathbf{I}]^{-1} \mathbf{y} \quad (\text{A1})$$

$$875 \quad cov_{post}(\mathbf{z}) = k(\mathbf{z}, \mathbf{z}) - k(\mathbf{z}, \mathbf{x}) [k(\mathbf{x}, \mathbf{x}) + \sigma_n^2 \mathbf{I}]^{-1} k(\mathbf{x}, \mathbf{z}) \quad (\text{A2})$$

where \mathbf{I} is the identity matrix. These equations can be interpreted as follows. The posterior mean is a linear combination of observations \mathbf{Y} and the process covariances between positions of the available observations and the new position $k(\mathbf{z}, \mathbf{x})$. Usually, the kernel is assumed to decrease with increasing separation between locations. This implies that when the new position \mathbf{z} is out of the range of available observations, the posterior mean will tend towards the prior mean. The posterior 880 variance is smaller than the prior variance, since the available observations reduce the range of likely values of $f(\mathbf{z})$.

Appendix B: Metrics of TCnpp ensemble members

Distribution of skill metrics for the ensemble of reconstructions with noisy MPIESM pseudoproxies with (a) the full emGPR, (b) the sparse emGPR and (c) PCR. The histograms show the respective distributions, the vertical lines correspond to the metric of the ensemble mean noted also in Fig. 4. The printed numbers denote the minimum and maximum of the respective metrics and correspond to the ensemble ranges given in the text.

Appendix B: CCSM4 pseudoproxies

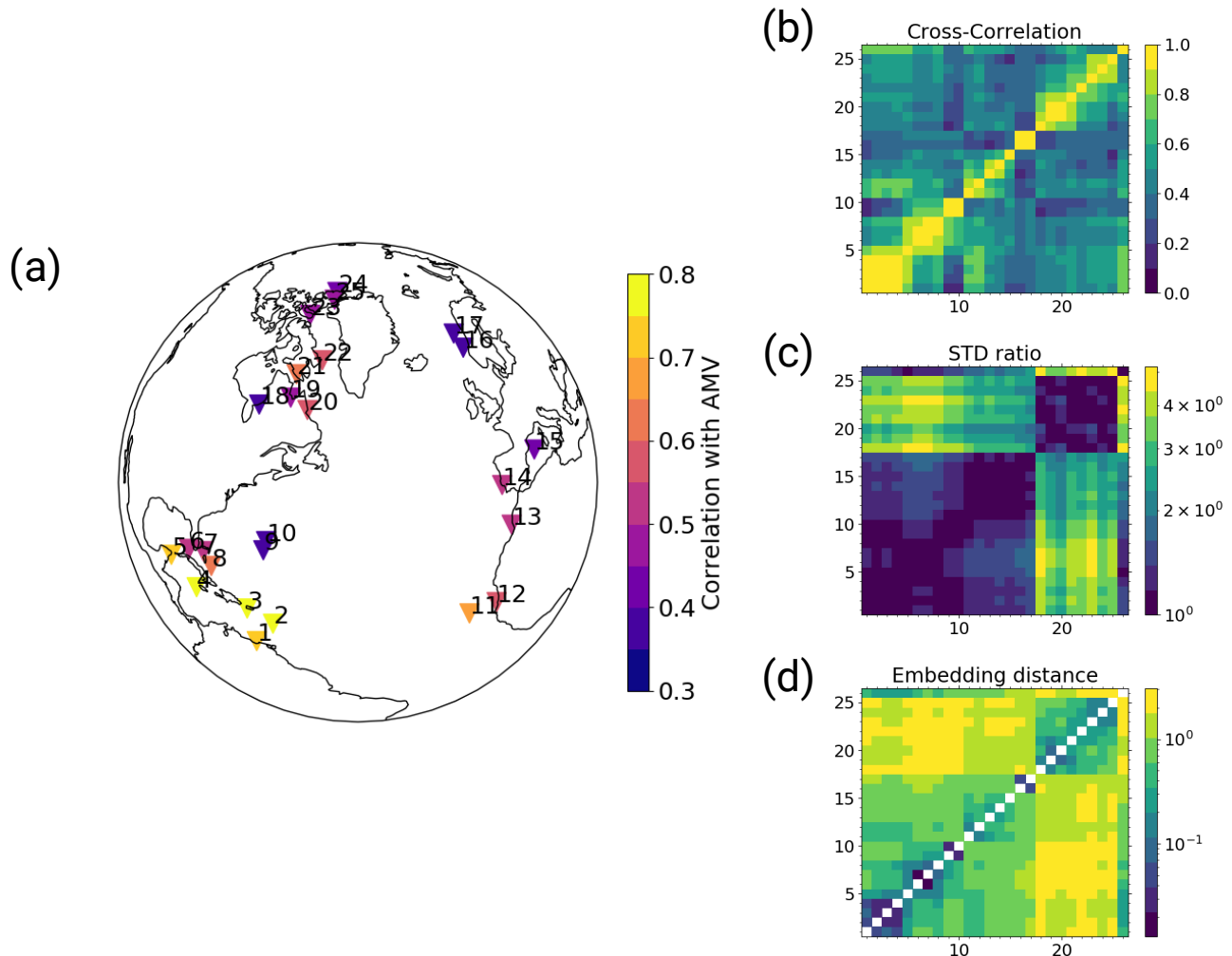


Figure B1. The selected pseudoproxy records and resulting distance metrics based on the CCSM4 simulation. **(a)** the locations of the records, colour-coded with the correlation between the records and the AMV during the last 150 simulation years (after detrending); **(b)** cross-correlation; **(c)** standard deviation ratio and **(d)** the resulting embedding distances from the combination of both. Matrix indexes 1 to 25 are the selected pseudo proxy records as labeled in (a), index 26 is the simulated AMV index. The diagonal entries in (d) are left empty because zero cannot be displayed on the logarithmic color scale.

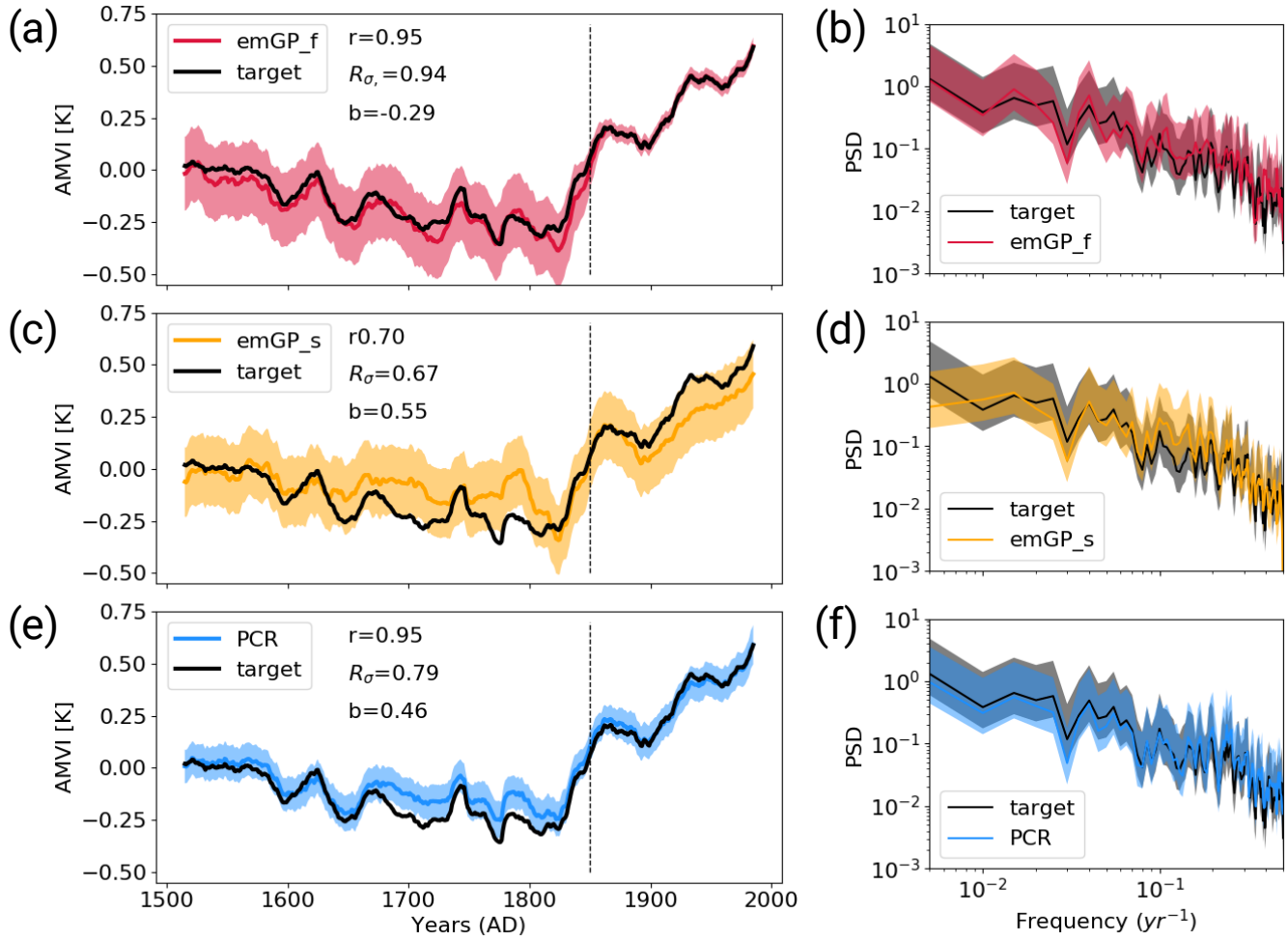


Figure B2. Reconstructions with perfect CCSM4-pseudoproxies based on **(a,b)** the full emGPR, **(c,d)** the sparse emGPR **(e,f)** PCR. Left-hand panels show the smoothed reconstructed and target timeseries. The dashed line marks the separation between training and testing periods. Shading indicates the 95% confidence interval. The metrics r , R_σ and b denote correlation, the ratio of standard deviations and the bias relative to the target standard deviation, respectively. Subscripts sm and yr denote smoothed and unsmoothed data, respectively. The metrics are calculated for the reconstruction period (1500 to 1850). Right-hand panels show the Welch powerspectra of the target and reconstructed AMVI. Shading indicates the 95% confidence interval. The power spectral density (PSD) is given in $K^2 yr$.

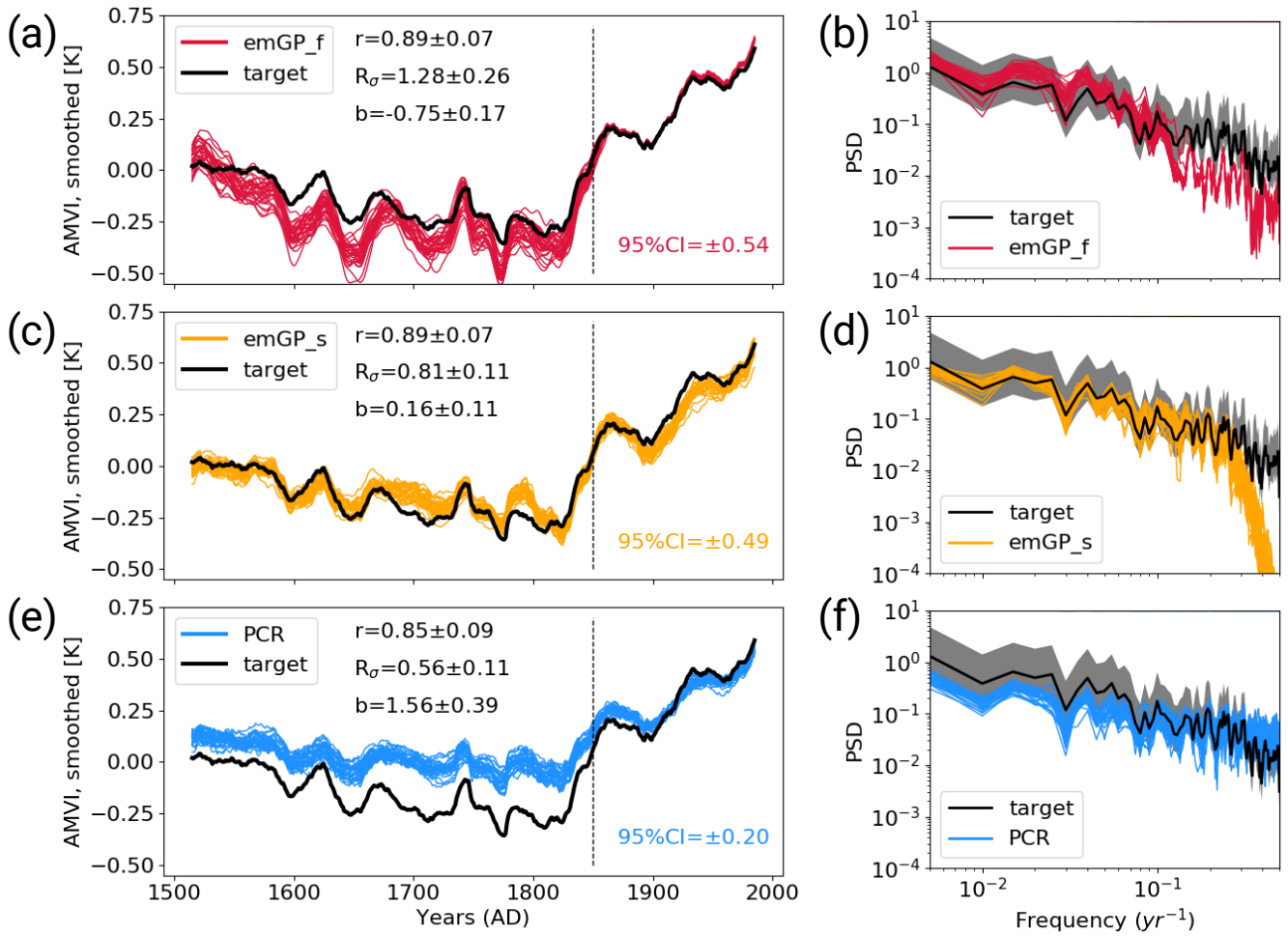


Figure B3. Reconstructions with noisy CCSM4-pseudoproxies based on (a,b) the full emGPR, (c,d) the sparse emGPR (e,f) PCR. Left-hand panels show the smoothed reconstructed and target timeseries. The dashed line marks the separation between training and testing periods. Thin lines show the individual ensemble members, the bold line indicates the ensemble mean. The metrics r , R_σ and b denote correlation, ratio of standard deviations and the bias relative to the target standard deviation, respectively. Subscripts sm and yr denote smoothed and unsmoothed data, respectively. The metrics are calculated for the ensemble mean during the reconstruction period (1500 to 1850). Right-hand panels show Welch powerspectra of the target and reconstructed AMVI. Thin lines indicate the spectra of the individual ensemble members, the bold line indicates the spectrum of the ensemble mean. Shading indicates the 95% confidence interval of the ensemble mean spectrum. The power spectral density (PSD) is given in $\text{K}^2 \text{yr}$.

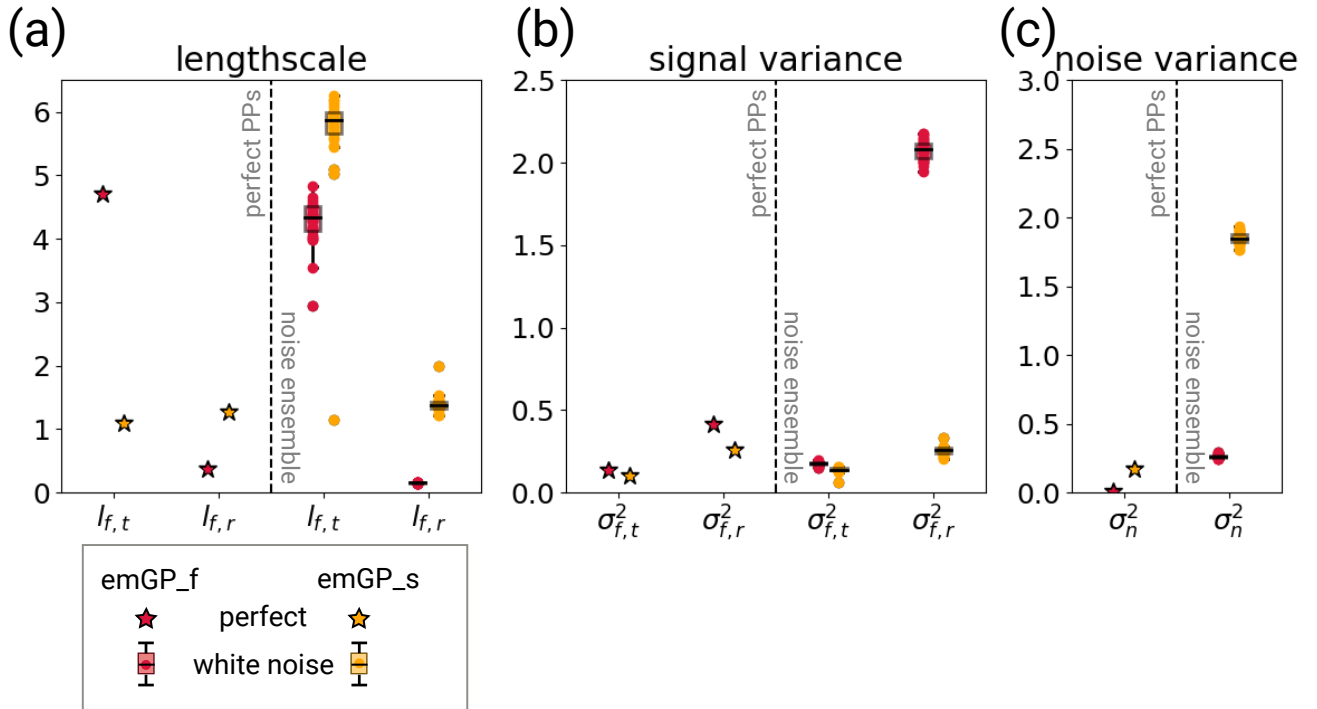


Figure B4. The respective hyperparameters for different training periods with CCSM4-based perfect pseudoproxies (left halves of the panels) and the different white noise ensemble members (right halves of the panels). The hyperparameters are (a) the typical lengthscales $l_{f,t}$ and $l_{f,r}$, (b) the signal variance $\sigma_{f,t}^2$ and $\sigma_{f,r}^2$, and (c) the noise variance σ_n^2 . The subscript t indicates that the kernel operates only on the time dimension; the subscript r indicates that the kernel operates on all dimensions, including time (see Eq. 6 and 7). The lengthscales are unitless, corresponding to the unitless distance of the embedding space. The lengthscale $l_{f,t}$ can be transformed into years through division by 1.10. The signal and noise variance are given in K^2 .

Appendix C: Metrics of TCnpp ensemble members

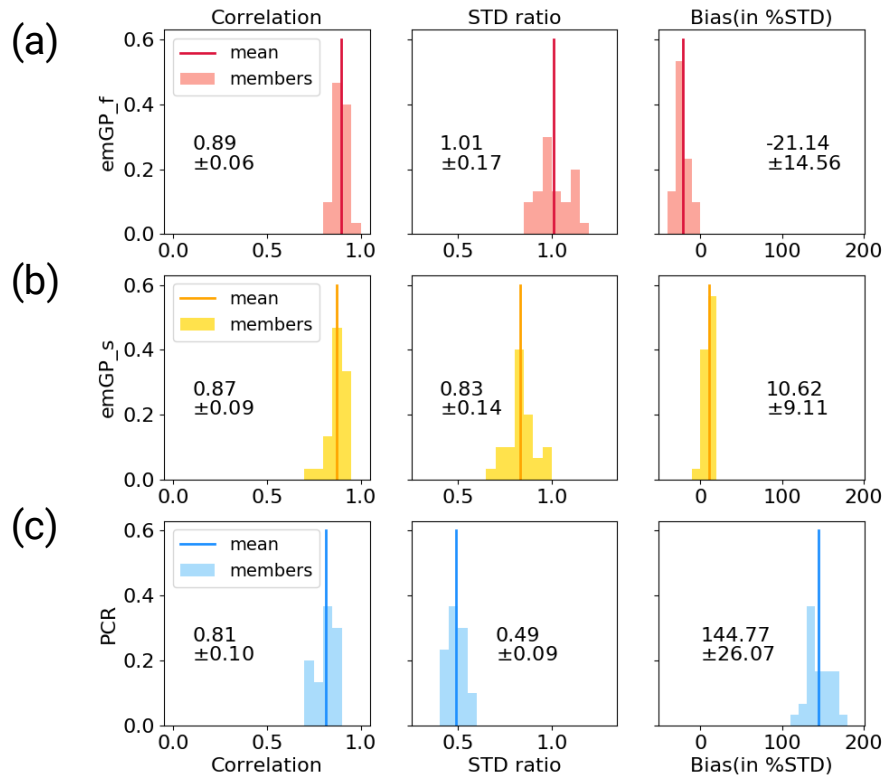


Figure C1. Distribution of skill metrics for the ensemble of reconstructions with noisy MPIESM-pseudoproxies with (a) the full emGPR, (b) the sparse emGPR and (c) PCR. The histograms show the respective distributions, the vertical lines indicate the ensemble mean. The printed values denote the mean and spread (2σ) which are also reported in the text and Fig. 4.

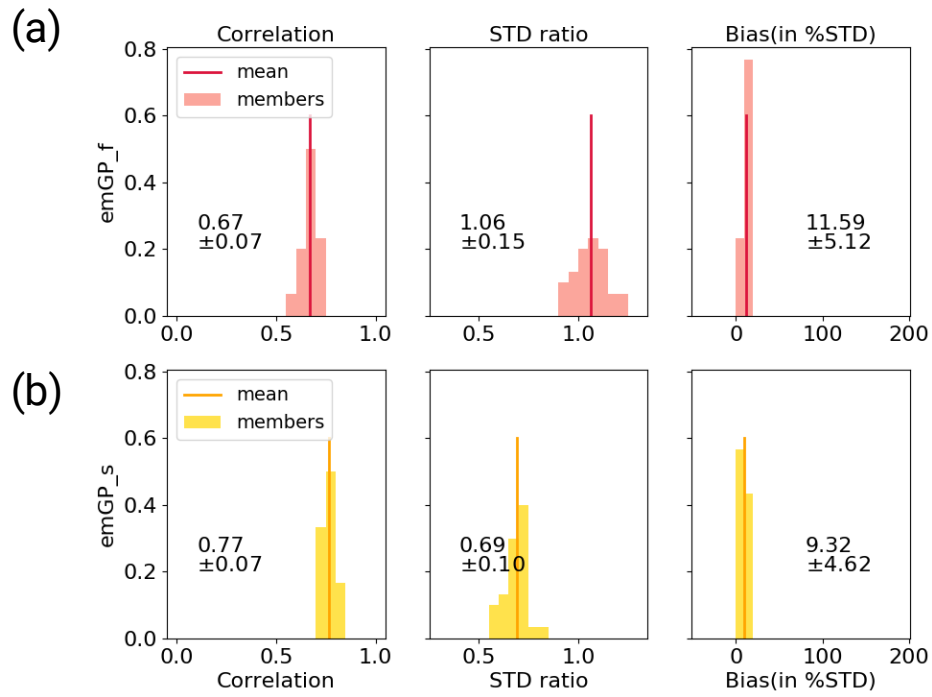


Figure C2. Distribution of skill metrics for the ensemble of reconstructions with noisy MPIESM-pseudoproxies and realistic data-availability with (a) the full emGPR and (b) the sparse emGPR. The histograms show the respective distributions, the vertical lines indicate the ensemble mean. The printed values denote the mean and spread (2σ) which are also reported in the text, Fig.6 and Fig.7.

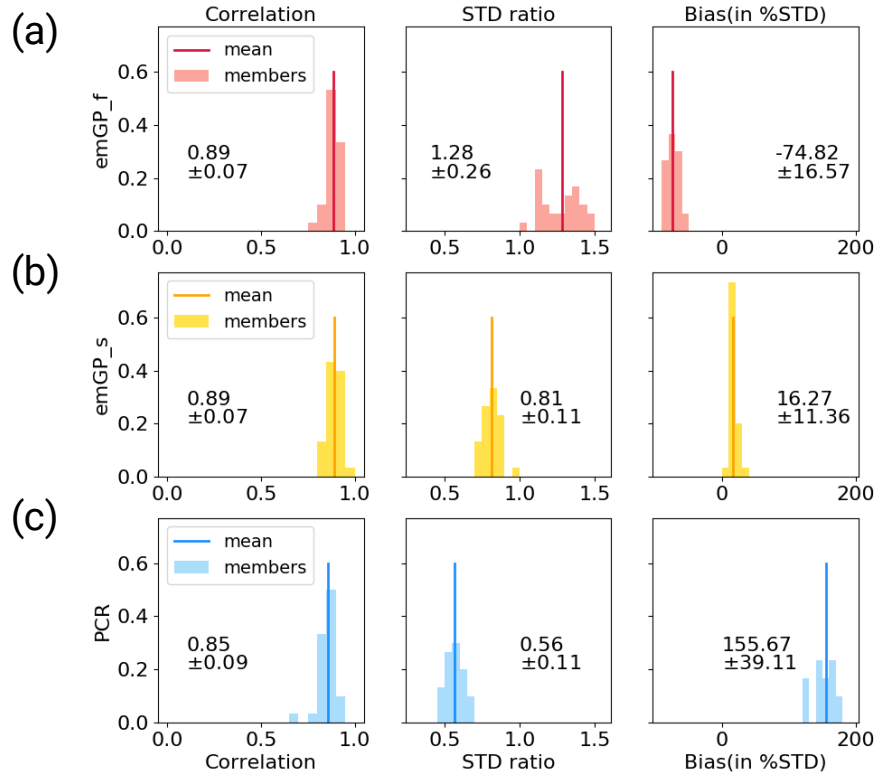


Figure C3. Distribution of skill metrics for the ensemble of reconstructions with noisy CCSM4-pseudoproxies with (a) the full emGPR, (b) the sparse emGPR and (c) PCR. The histograms show the respective distributions, the vertical lines indicate the ensemble mean. The printed values denote the mean and spread (2σ) which are also reported in the text and Fig. B3.

Appendix D: Sensitivity experiments

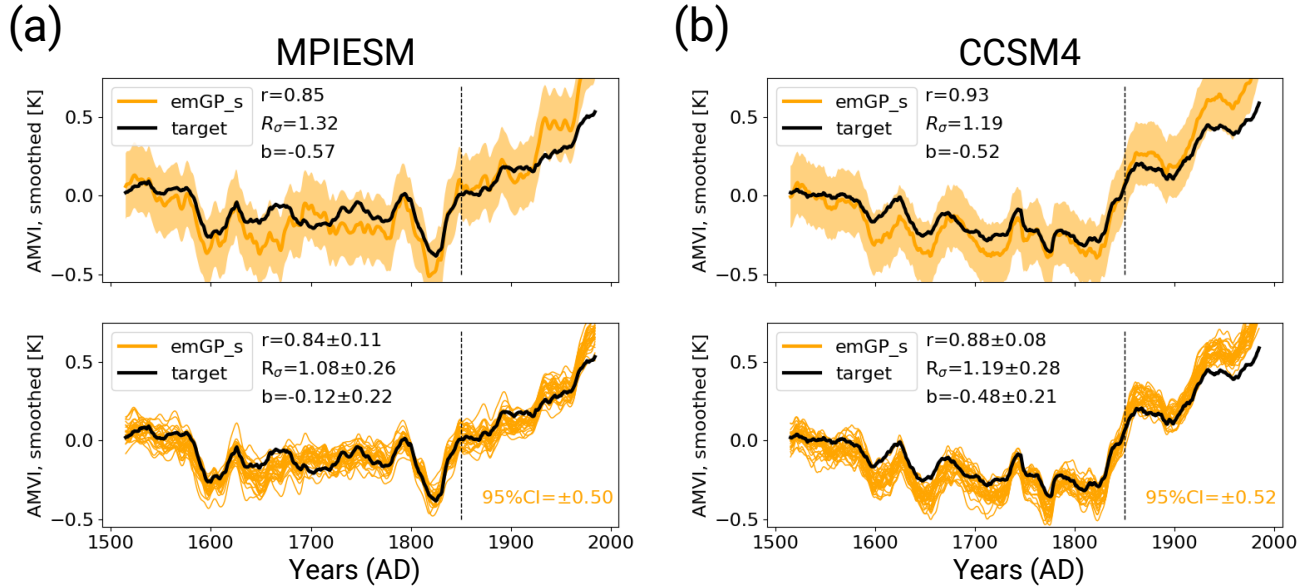


Figure D1. Sensitivity experiments similar to TC_{ppp} and TC_{npp} with the sparse emGP but with only half the number of pseudoproxies. Reconstructions based on (a) eleven MPIESM-based pseudoproxies and (b) twelve CCSM4-based pseudoproxies. The upper panels show the reconstruction with perfect pseudoproxies, the lower panels show the reconstruction with noisy pseudoproxies.

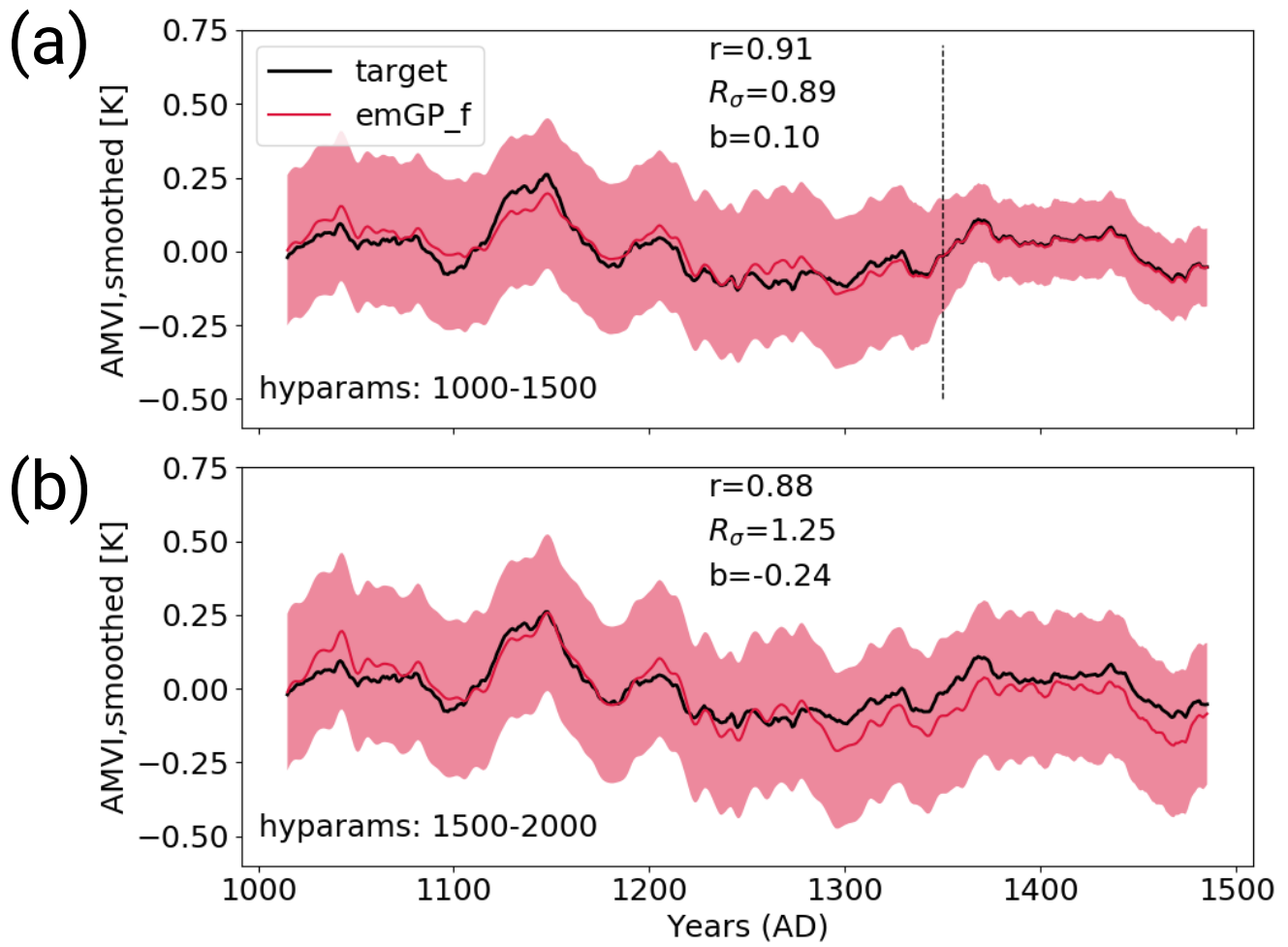


Figure D2. (a) Sensitivity experiment similar to TCp2k with the full emGP but the hyperparameters are estimated for the period 1000-1500, where the proxy availability is strongly reduced (see Fig. 1b). The AMVI during the years 1350-1500 has been used for training. (b) AMVI reconstruction for the same period from Fig. 6b for comparison. Here, the hyperparameters were estimated for the period 1500-2000.

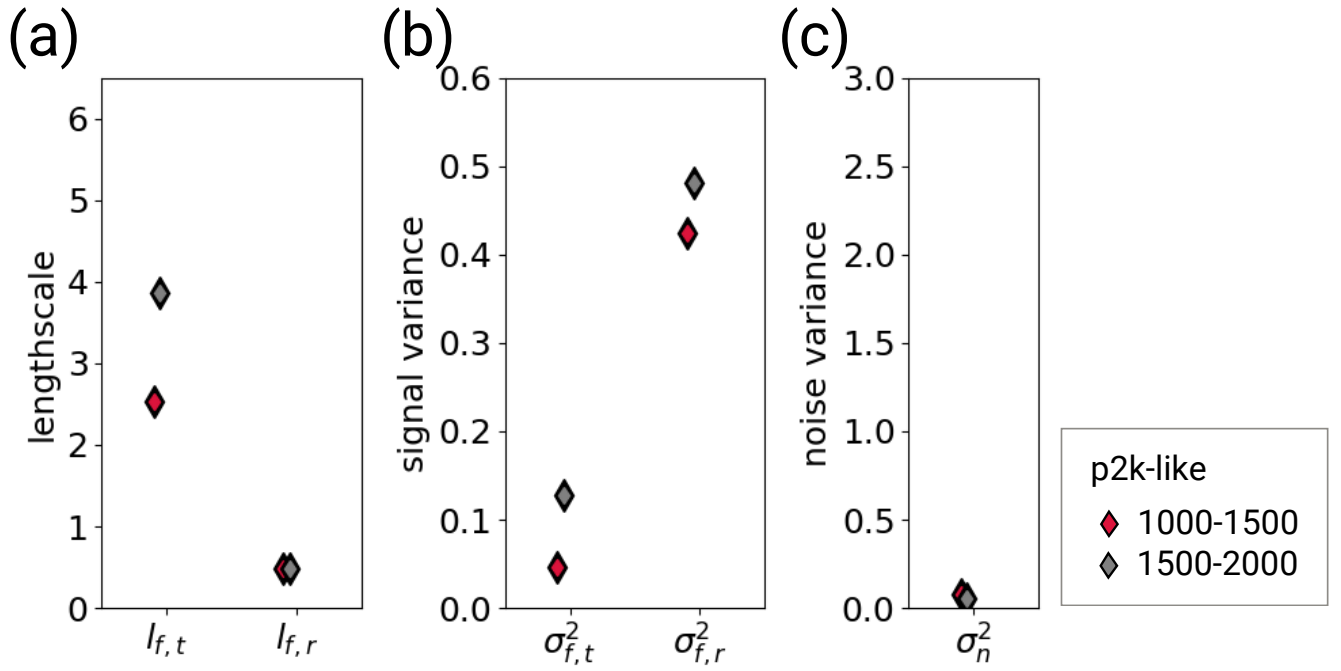


Figure D3. Hyperparameters of the sensitivity experiment shown in Fig.D2. Red diamonds correspond to the period 1000-1500, grey diamonds to the period 1500-2000 (grey diamonds here are the same as the red diamonds in Fig. 5). The hyperparameters are (a) the typical lengthscales $l_{f,t}$ and $l_{f,r}$, (b) the signal variance $\sigma_{f,t}^2$ and $\sigma_{f,r}^2$, and (c) the noise variance σ_n^2 . The subscript t indicates that the kernel operates only on the time dimension; the subscript r indicates that the kernel operates on all dimensions, including time (see Eq. 6 and 7). The lengthscales are unitless, corresponding to the unitless distance of the embedding space. The lengthscale $l_{f,t}$ can be transformed into years through division by 1.10. The signal and noise variance are given in K^2 .

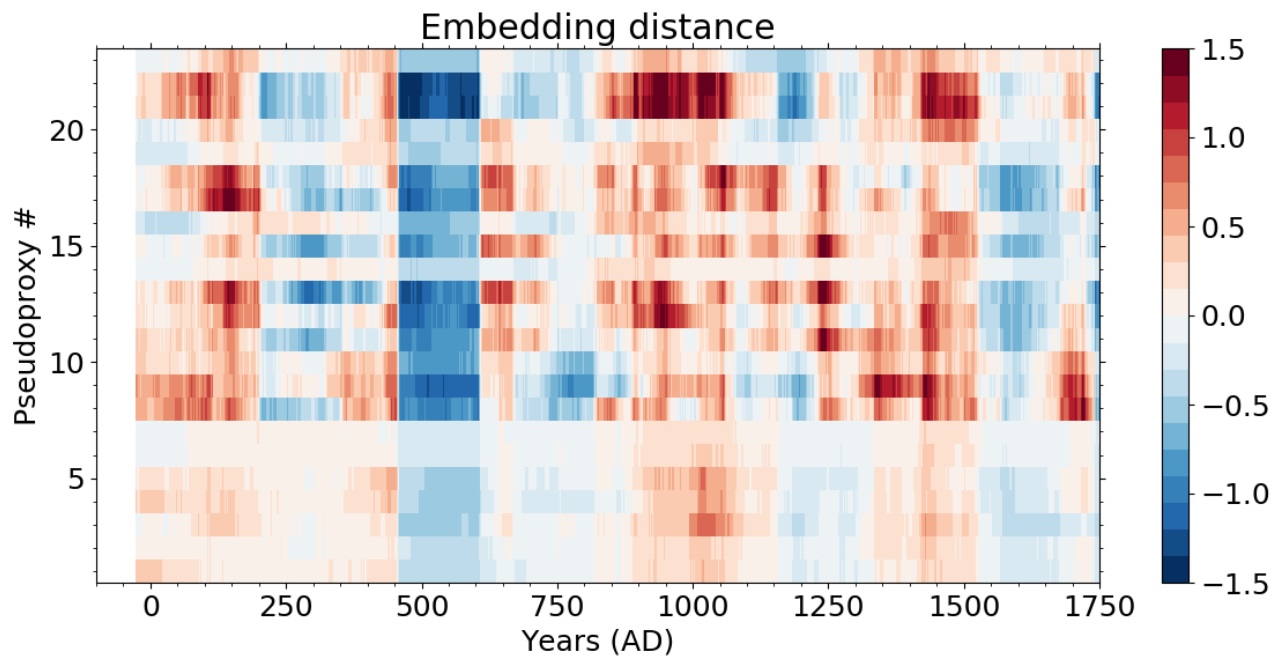


Figure D4. Changes of the embedding distance between the AMVI and the pseudoproxy records (Eq. 5) calculated over a running window of 151 years. The anomalies are calculated against the mean distance over the entire period. Blue shading indicates a smaller distance, i.e., more similar records. Red shading indicates a greater difference, i.e., less similar records. The numbers on the y-axis are the correspond to the pseudoproxy numbering in Fig. 1.